Spectrally Selective High Detectivity Uncooled Detectors for the Long Wave Infrared

A DISSERTATION

SUBMITTED TO THE FACULTY OF THE GRADUATE SCHOOL

OF THE UNIVERSITY OF MINNESOTA

BY

Anand Sudhir Gawarikar

IN PARTIAL FULFILLMENT OF THE REQUIREMENTS

FOR THE DEGREE OF

Doctor of Philosophy

Joseph John Talghader

May, 2013

Acknowledgements

This dissertation was possible due to the support of several people. First and foremost, I would like to express my gratitude to my adviser Dr. Joey Talghader for guiding me through graduate school and for his patience through all its ups and downs. My colleague Ryan Shea was a partner in this research and his contributions were instrumental in its successful completion. I would like to sincerely thank him for his efforts towards this project. Funding support for my graduate work came from various sources including DARPA, Army Research Office, Penn State Electro-Optics Center and University of Minnesota Graduate School and is gratefully acknowledged.

Many colleagues, past and present, helped me along the way. I would like to thank Brad Tiffany, Jan Makowski, Nick Gabriel, Merlin Mah, Wing Chan, Sangho Kim, Luke Taylor, Kyle Olson and Andrew Brown for all the help over the years. I would also like to acknowledge the staff at the Nanofabrication Center, University of Minnesota for their valuable assistance during device fabrication. I would also like to thank my friends Apurva Somani, Saurabh Tewari, Kalpesh Singal, Gagan Aggarwal and Govind Saraswat for providing respite when the research got too difficult.

Finally, I would like to thank my parents Rekha and Sudhir Gawarikar for their love and support and Sonali for her encouragement and understanding.

Dedication

To my parents, Rekha and Sudhir Gawarikar.

कर्मण्येवाधिकारस्ते मा फलेषु कदाचन ।
मा कर्मफलहेतुर्भूर्मा ते सङ्गोऽस्त्वकर्मणि ॥ २-४७॥

Your right is to action only, never to the fruits of action.
Let not the fruits of action be your motive,
nor let your attachment be to inaction.

Bhagvad Gita, 2-47

Abstract

Long wave infrared is an important region of the electromagnetic spectrum due to strong thermal emission in this region by room temperature blackbodies and good atmospheric transparency which enables transmission of electromagnetic energy over large distances. Detectors for this spectral region, especially ones that can operate at room temperature, have been an active area of research due to applications in surveillance, remote sensing and chemical detection. Of particular interest is the integration of spectral and spatial filtering directly with the detector to incorporate multispectral capabilities with reduced hardware complexity.

This thesis explores several aspects of spectral selectivity in infrared detectors operating at room temperature. The effects of spectral selectivity on the fundamental photon noise limit are first explored using the formalism of an ideal resonant optical cavity. It is shown that the photon noise limit of such a detector is higher than that of a broadband detector. The theoretical performance of this detector architecture is investigated for the specific application of passive standoff detection of gases.

Some practical aspects and trade-offs involved in optical and electrical design of such detectors is discussed in detail. A process for fabrication of these detectors using standard silicon micromachining techniques is described. Various optical and electrical characterization techniques are used to demonstrate spectrally selective high sensitivity detectors operating at room temperature. These detectors have amongst the highest sensitivities reported in the literature.

Finally, a thermal model for detector responsivity is developed for the particular case of spatially non-uniform absorption. An approximate expression for detector absorbing area is derived from this model, which can be directly substituted in standard equations to estimate responsivity to good accuracy. Detailed derivation and experimental verification of this model is described.

Contents

List of Tables

List of Figures

Chapter 1

Introduction

Electromagnetic radiation is emitted by any body at temperature above absolute zero, the spectral distribution of which is described by Planck's radiation law. The peak wavelength of the emitted radiation from a thermal radiator depends on its temperature and is frequently in the infrared region of the spectrum for common terrestrial objects. In particular, the peak wavelength of radiation emitted by a body at room temperature lies around 10 μm wavelength. The region of the spectrum between 8 μm and 12 μm is also an atmospheric transmission window due to minimal absorption from carbon dioxide and water vapor molecules. Thus radiation emitted by thermal sources in this wavelength range can be detected from a distance. This region is sometimes referred to as the thermal infrared or long wave infrared (LWIR) band. Since observation of thermal radiation does not require any auxillary illumination, this band has been commonly used for surveillance and remote sensing applications.

Detection of radiation in the LWIR is challenging because of the low energy of the radiated photons (of the order of 0.1 eV). Two classes of detectors have been developed for this purpose. Photon detectors respond to individual photons to excite electron-hole pairs through inter-band or inter-sub-band processes in semiconductors to generate a photocurrent. These detectors which include low bandgap compound semiconductors like HgCdTe and quantum well infrared photodetectors (QWIPs), require cooling for operation in order to suppress thermal excitation of carriers across the band gap. The second class of detectors are known as thermal detectors since

they directly measure the energy of incoming photons through a change in temperature of the detector material. The actual electrical transduction involves measurement of the temperature change through a variety of physical effects like resistance change (resistive bolomters), Seebeck effect (thermopiles) and pyroelectric effect amongst others. These detectors are relatively simple to fabricate and do not require any cooling to operate.

Uncooled long wave infrared detectors have seen great advancements in technology in the previous few decades. The elimination of cooling hardware and the use of silicon microfabrication techniques have made it possible to manufacture dense two dimensional arrays integrated with electronics in a cost effective manner [3, 4]. This is a distinct advantage over photon detectors where arrays are cost prohibitive to produce and single pixel detectors are more common. Current state of the art commercial thermal detectors are vanadium oxide based resistive bolometers and are used for applications in night vision and radiometry [5].

In the traditional radiometry applications the objects under observation tend to a have broad thermal emission spectrum as described by Planck's law. But there are other applications where the object under observation has narrow spectral distribution. An example would be molecular spectroscopy using vibrational and rotational resonances of molecules which lead to characteristic absorption signatures in the infrared. A related example would be analysis of emission from hot exhaust gases and fumes. Detection of such narrow sources require the use of filters to restrict detector response to the useful range.

In addition to spectral filtering, high performance spectroscopy systems often require cold shielding to restrict the detector field of view. This is necessary because the object under observation has a finite geometric extent and if observed from a distance, the radiated power lies within a small solid angle. Radiation from bright objects in the background outside the useful acceptance angle can degrade the system sensitivity by increasing clutter. Such high performance systems involve integration of filters, cold shields and scanning systems with the actual detectors and can be incredibly complex. Cooled photon detectors are the instruments of choice for such systems because uncooled thermal detectors have lower sensitivity than their cooled photon detector counterparts.

Further improvements in sensitivity are desirable if these detectors are to be useful for high

performance spectroscopy applications. Improvements in detector sensitivities have been obtained through a combination of thermal conductance reduction [6], improved transducer materials [7, 8] and reduction in the detector noise [9]. Due to the small magnitude of their 1/f noise, thermopile detectors have an advantage over resistive bolometers and are more suitable for high detectivity applications.

There has been a sustained effort within the infrared detector community towards integrating filters directly with detector pixels towards a goal of achieving multispectral detection systems at reduced system complexity, size and cost [10]. In the case of thermal detectors the electrical transduction is unaffected by the operating wavelength range, and the optical absorption structures can be independently optimized to cover a variety of spectral bands. Spectrally selective absorption has been demonstrated in infrared detectors and filters using patterned metamaterials [11, 12] and resonant optical cavities [13, 14, 15].

The reduction of undesirable background absorption through spectral and spatial filtering can lead to improvement in detector sensitivity at a very fundamental level. The ultimate limit to detector performance is due to noise introduced by fluctuations in incoming photons. This is called the photon noise limit or the background noise limit. This limit is extrinsic to the detector and exists even when the detector is ideal in all respects. Detectors used in applications requiring extreme accuracy and sensitivity, for example in cosmological instruments, usually operate in this background limited regime [16].

The theory of photon noise for thermal detectors has been derived under the assumption of a uniform broadband absorption. The background noise limit thus derived has been accepted as the ultimate limit of performance of room temperature thermal detectors. If the assumption of a broadband detector absorption is relaxed, the photon noise limit of thermal detector sensitivity is found to be higher than that assumed conventionally.

This thesis explores several aspects of spectrally selective absorption in thermal detectors in detail. Using numerical simulations it is first shown that photon noise for a spectrally narrowband detector can be lower than a detector with broadband absorption. Next, a thermal detector that utilizes resonant cavity coupling and low noise thermoelectric readout scheme is demonstrated to achieve high detectivity values. This detector has amongst the highest room temperature detectivity values published in the literature. The detectivity value is within an

order of magnitude of the broadband photon noise limit and can be potentially scaled to sensitivities beyond that limit through improvements in detector design and fabrication process outlined in this thesis. Finally a convenient approximation to correctly estimate detector performance with spatially non-uniform absorption is also presented.

1.1 Thesis organization

The thesis is divided into the following chapters.

- Chapter 2 contains a detailed discussion of the photon noise limit of thermal detectors. The photon noise limit under narrowband conditions is first explored analytically and using numerical simulations and is shown to be much higher than those of broadband absorption detectors. A narrow band detector architecture utilizing resonant cavity absorption is used for these simulations. The performance of this detector architecture is then simulated for a specific application.

- Chapter 3 gives the details of design and fabrication of resonant absorption optical cavities including two specific examples. A technique for measuring optical constants of thin films in the infrared is described. Details of the process for fabricating these resonant optical cavities is discussed.

- Chapter 4 gives the details of design, fabrication and characterization of spectrally selective thermal detectors using optical designs from chapter 3 and thermoelectric readout. Significant portions of the work described in this chapter was performed in collaboration with Ryan Shea. Some aspects of general thermal detector design are first presented. A detailed fabrication process flow for these detectors is then described. Optical and electrical characterization results for some detectors are then presented along with the instrumentation details.

- Chapter 5 gives details behind an approximate method used for detector characterization when its actual absorbing area is not well defined or when there are multiple light sensitive regions with different absorptivities. This approximation is useful for correctly estimating

the responsivity of the detectors fabricated in chapter 4 without the need for accurately defining the incident spot size using optical techniques.

Chapter 2

Photon noise in narrowband thermal detectors

Vibrational and rotational resonances give rise to characteristics absorption signatures for many molecules in the infrared and form the basis of infrared spectroscopy for the identification and quantitative measurement of these molecules. Fourier-Transform infrared spectrometers are commonly used for such measurements due to their high throughput, speed of measurement, narrow spectral resolution and good accuracy. These advantages are a result of several decades of instrument development and have made FTIR spectrometer the instrument of choice for infrared spectroscopy.

In particular, an FTIR system has the advantage of higher throughput compared to a sequential wavelength scanning instrument. This is due to its ability to measure many spectral windows simultaneously in a given measurement time window. This is called the multiplexed advantage or the Fellgett advantage, and has been discussed extensively [17]. In this chapter, the multiplexed advantage of an FTIR system is first discussed, especially under the conditions of photon noise. It is shown that the under complete photon noise limited condition an FTIR system has no advantage over a scanning system. Next, the photon noise limit for a narrowband thermal detector are discussed. Finally, the theoretical performance of an ideal narrowband thermal detector limited by photon noise is evaluated for a specific application, that of passive

detection of gases at a distance.

2.1 The multiplexed advantage

The multiplexed advantage of a Fourier Transform instrument, which arises from the ability of an FTIR system to simultaneously measure across all the spectral bands in its measurement time window, was first derived by Fellgett [18] and hence is also called the Fellgett advantage. This is unlike a grating spectrometer which sequentially scans wavelength bands one at a time thus spending a fraction of its measurement time in each spectral band.

Besides the multiplexed advantage, an FTIR system also has a throughput advantage over a grating instrument due to the limited light gathering capacity from narrow slits, known as the Jacquinot advantage [17]. Tha Jacquinot advantage does not apply for a wavelength scanning Fabry-Perot interferometer due to lack of entrance and exit slits. These advantages are clearly valid in case of single pixel detector instruments. If an array of equivalent detectors were available, then a scanning instrument like a grating spectrometer could in principle, perform a spatially multiplexed measurement and there is some debate about the exact magnitude of these advantages in imaging spectrometers [19, 20, 21].

A common example of sequential scanning instrument is a diffraction grating followed by a slit. The performance analysis in this section, though specifically referred to for a grating, is general enough be applicable to other sequential scanning arrangements. Following the analysis of Hirschfeld [22] we can write for a signal spectral density $f(\nu)$, the signal to noise ratio (SNR) of a grating system measuring the signal over time t can be given by

$$SNR_G = \frac{f(\nu)\Delta\nu E_G t^{1/2}}{a}\left(\frac{\nu_{max}-\nu_{min}}{\Delta\nu}\right)^{-1/2} \tag{2.1}$$

where $\Delta\nu$ is the spectral resolution of the grating, E_G is the grating efficiency, t is the measurement time, a is the detector electrical noise and $\nu_{max}-\nu_{min}$ is the spectral range of the measurement. .

The quantity $N = (\nu_{max}-\nu_{min})/\Delta\nu$ gives the number of wavelength bands (resolution elements) of the instrument. For a detector noise limited detectivity $D* = \sqrt{A_d}/a$ the SNR can

be written as

$$SNR_G = \frac{f(\nu)\Delta\nu D^* E_G t^{1/2}}{\sqrt{A_d}} \left(\frac{\nu_{max} - \nu_{min}}{\Delta\nu}\right)^{-1/2} \tag{2.2}$$

Since an FTIR system measures all spectral bands for the entire time t, its SNR can simply be written as

$$SNR_F = \frac{f(\nu)\Delta\nu E_F t^{1/2}}{a} \tag{2.3}$$

where E_F is typically the efficiency of the interferometer beam splitter. Comparing a grating system to an FTIR system for equal efficiencies and equal measurement times, the ratio ζ of the SNR of an FTIR to a grating system is given by

$$\zeta_d = \frac{SNR_F}{SNR_G} = N^{1/2} \tag{2.4}$$

This is exactly the Fellgett advantage. Hence under detector noise limited conditions the FTIR will have an advantage of $N^{1/2}$ over a grating system.

Under photon noise limited conditions this advantage is no longer observed because the FTIR system redistributes the photon noise the entire spectral range since all the spectral bands are being observed at the same time. This is not the case for a grating system since the detector now only detects the noise that lies within the spectral band filtered by the grating. The SNR under photon noise limited conditions can be written as

$$SNR_G = \frac{f(\nu)\Delta\nu)}{\left[a^2 + b^2 f^2(\nu)\Delta\nu^2\right]^{1/2}} E_G t^{1/2} N^{-1/2} \tag{2.5}$$

where b gives the magnitude of the photon noise. For an FTIR the photon noise is spread across all frequencies giving

$$SNR_F = \frac{f(\nu)\Delta\nu)}{\left[a^2 + b^2(\int_{\nu_{max}}^{\nu_{min}} f(\nu)d\nu)^2\right]^{1/2}} E_F t^{1/2} \tag{2.6}$$

Under the assumption that the spectral density is uniform across the entire range such that

$f(\nu) = f_0$ then the multiplexed advantage is given by

$$\zeta_{ph} = \left[\frac{a^2 + b^2 f_0^2(\nu)\Delta\nu^2}{a^2 + b^2 f_0^2(\nu_{max} - \nu_{min})^2}\right]^{1/2} \frac{E_F}{E_G} \frac{1}{N^{-1/2}} \tag{2.7}$$

Substituting $g = bf_0\Delta\nu/a$ and noting that $\nu_{max} - \nu_{min} = N\Delta\nu$ we can finally write

$$\zeta_{ph} = \left[\frac{1 + g^2}{N^{-1} + Ng^2}\right]^{1/2} \tag{2.8}$$

This equation gives the multiplexed advantage under conditions when photon noise is comparable to the electrical noise. The advantage ζ_{ph} is a function of the noise magnitude and the number of spectral bands that are scanned. It can also be seen that when $g = N^{-1/2}$ then $\zeta_{ph} = 1$ and the multiplexed advantage disappears. Under the extreme condition that detector electrical noise is negligible compared to the photon noise, i.e. when $g \to \infty$

$$\zeta_{ph} = \left[\frac{1}{1 + N}\right]^{1/2} \tag{2.9}$$

This shows that the SNR of an FTIR will always be degraded compared to a scanning instrument when the system is completely dominated by the photon noise. Note that this is valid under the simplifying assumption of a uniform spectral density. This assumption is invalid when viewing bright emission lines, in which case the use of equation 2.6 is more appropriate.

Also, this analysis assumes that all sources of photon noise seen by the detector pass only through the interferometer or the grating slits. This is equivalent to saying that the detector has a radiation shield that restricts its field-of-view to one that matches the output of the interferometer and that no sources outside this field-of-view contribute to the photon noise. This assumption would not be valid in case of an uncooled thermal detector which would have an unrestricted hemispherical field-of-view containing large noise generators.

There are several architectures are possible for constructing a photon noise limited detector coupled to a sequential wavelength scanning filter. One such design is a thermal detector resonantly coupled to a scanning optical interferometer. Thermal detectors are an attractive choice

for room temperature operation and integration of the detector directly with an optical interferometer reduces the system complexity. The photon noise characteristics of such a narrowband thermal detector system are discussed in the next section.

2.2 Photon noise limit

The fundamental upper limit of sensitivity of a radiation detector is determined by the statistical fluctuations in the radiation exchange between the detector and its surroundings [23, 24, 25]. A detector operating at this upper limit is said to be background-limited. Background-limited performance has traditionally been achieved by cooling below room temperature. For photon detectors it is known that, once thermal generation and other noise sources have been suppressed, the detectivity is primarily governed by the overlap of background thermal emission with the spectral response of the detector [26].

The fundamental theory of photon noise in thermal detectors has been developed assuming structures with a spectrally uniform high absorption. It has been postulated previously that introducing radiation shielding tor restrict the detector field of view can lead to improvement in the photon noise limited detectivity but the spectral dependence of the detector itself is neglected [27]. From the point-of-view of the received signal this seems perfectly understandable since a uniform high absorption guarantees maximum light collection, but it also causes the detector to incur maximum photon fluctuation noise even when the desired signal is limited in spectral width or lies in a spectral region far from the maximum emission of the background.

One can develop a more general theory of the background fluctuation limit by realizing that the emissivity of a thermal detector may vary with direction and wavelength. Under this modification the background noise limit is found to be substantially reduced to that of a blackbody. Such wavelength and direction dependent emissivity can be realized using optical cavity coupling. The benefits of this detector architecture and the requirements on its performance will be explored analytically in context of background limited detection.

2.2.1 Photon noise theory

Photon noise occurs due to statistical fluctuations in the incoming stream of photons. This is a well understood phenomenon that has been explored by several authors especially in the astrophysics community [28, 29]. Photons follow Bose-Einstein statistics for which the mean square fluctuations in the number of photons per mode is given by

$$\langle (\Delta n)^2 \rangle = n + n^2 \tag{2.10}$$

where n is the number of photons per mode given by Planck's distribution function. For a source of emissivity η, optical path with transmissivity τ and detector with emissivity ϵ this is given by

$$n = \frac{\eta \tau \epsilon}{e^{h\nu/k_B T} - 1} \tag{2.11}$$

where ν is the mode frequency, k_B is the Boltzmann constant and T is the temperature. The number of modes N of one polarization and wavelength λ can be written as $N = A\Omega/\lambda^2$ for a detector with area A and solid angle of acceptance Ω.

A thermal detector responds to the power of the incoming photons unlike a photon detector which responds to the rate of incoming photons. The mean squared energy of the photon fluctuation is given by $h^2\nu^2\langle(\Delta n)^2\rangle$ for one mode. The total noise power spectrum summed over all frequencies is then given by [28]

$$\begin{aligned} \langle P_n^2 \rangle &= 2 \int h^2\nu^2 \cdot 2N \cdot \langle (\Delta n)^2 \rangle \\ &= 4h^2c^3A \int_\lambda \int_\Omega \frac{\epsilon(\lambda,\Omega)}{\lambda^6(e^{hc/\lambda k_B T} - 1)} \left[1 + \frac{\epsilon(\lambda,\Omega)}{e^{hc/\lambda k_B T} - 1}\right] \, d\lambda d\Omega \end{aligned} \tag{2.12}$$

where $\epsilon(\lambda, \Omega)$ is the wavelength and direction dependent emissivity. If a detector has high emissivity inside its acceptance solid angle Ω_0 and low emissivity outside of it, then the net emissivity can be written as a piecewise summation of two independent emissivites as

$$\epsilon(\lambda,\Omega) = \begin{cases} \epsilon_{in}(\lambda) & \text{for } \Omega \leq \Omega_0 \\ \epsilon_{out}(\lambda) & \text{for } \Omega > \Omega_0 \end{cases} \tag{2.13}$$

In this case the integral of equation 2.12 can simplified and written as a sum of two wavelength dependent integrals. For a blackbody absorber, $\epsilon(\lambda, \Omega) = 1$ and equation 2.12 reduces to $\langle P_n^2 \rangle = 8A\sigma k_B T^5$ where σ is the Stefan-Boltzmann constant.

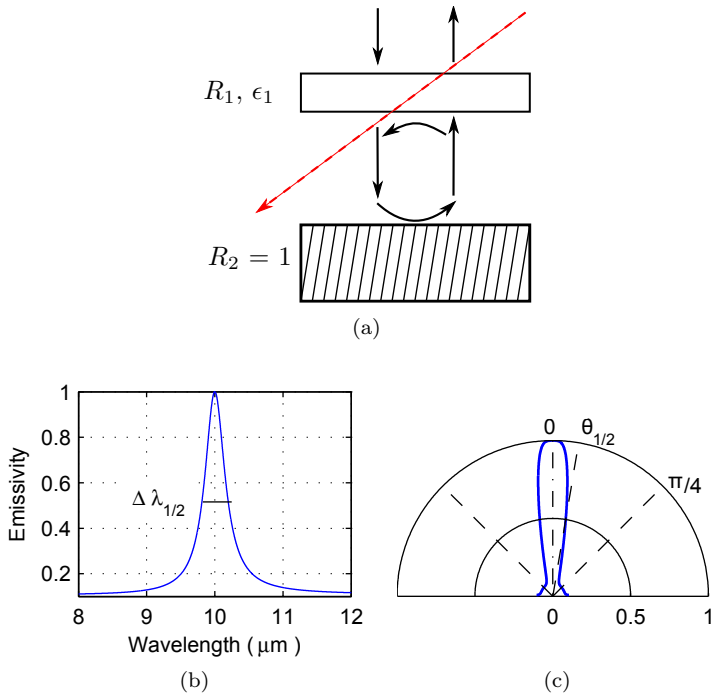

Figure 2.1: (a) Schematic of a cavity coupled absorber having direction dependent emissivity. (b) Emissivity as a function of wavelength. (c) Emissivity as a function of polar angle showing the acceptance angle of the cavity.

A direction and wavelength dependent emissivity can be implemented by a simple resonant cavity coupled structure as shown in Fig. 2.1a. This design is essentially a Fabry-Perot interferometer which consists of a low emissivity and high reflectivity absorber separated from a strongly reflecting back mirror by an m$\lambda/2$ air gap. The absorber can be integrated with an electrical readout scheme to realize an integrated thermal detector and scanning interferometer architecture. The reflectance of the cavity coupled structure is given by

$$R = \frac{r_1^2 + (1 - a_1^2)^2 - 2(1 - a_1^2) r_1 \cos(2\phi)}{1 + r_1^2 - 2 r_1 \cos(2\phi)} \tag{2.14}$$

where r_1 and a_1 are the field reflectivity and absorptivity of the top mirror and $\phi = 2\pi d \cos\theta/\lambda$

is the phase accumulated in a single traversal through the cavity. The absorption is localized at the top mirror and the gap between the two mirror is assumed to be completely transparent. A detailed derivation of this result is given in chapter 3. The cavity emissivity ϵ_{cav} equals absorptivity give by A = 1-R and is plotted against wavelength and incident angle in Fig. 2.1b and Fig. 2.1c for the condition that the front mirror emissivity and reflective are matched such that $\epsilon_1 = a_1^2 = 1 - r_1$.

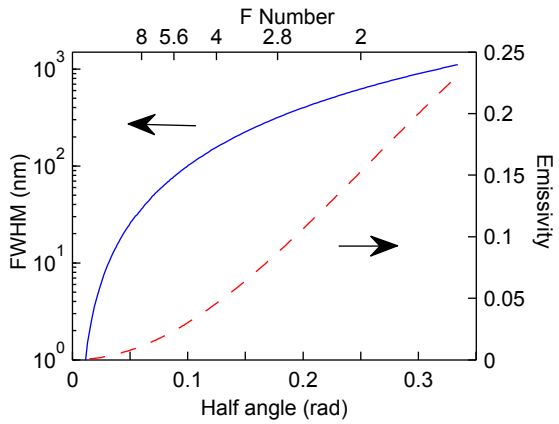

Figure 2.2: Plot of cavity Full Width Half Maximum and front mirror emissivity against the corresponding cavity half angle.

The cavity exhibits perfect emissivity only a specific resonance wavelength and only at normal incidence. The cavity full width half maximum $\Delta\lambda_{1/2}$ and cavity acceptance half angle $\theta_{1/2}$ are also indicated in the figures. For a finite size of the front mirror, the emissivity is angle dependent as shown in Fig 2.1c. The emissivity drops off rapidly due to walk off at non-normal incidence thus limiting its throughput.

The cavity resonance width and half angle can be engineered by selecting the appropriate value for front mirror reflectance and emissivity. Fig. 2.2 shows the variation of the cavity full width half maximum (FWHM) $\Delta\lambda_{1/2}$ with the corresponding cavity half angle as the front mirror emissivity is continuously varied. It can be seen that narrow resonances will restrict the cavity acceptance angles to small values and will require low emissivity and high reflectivity front mirror. Also at an oblique angle of incidence $\theta > \theta_{1/2}$ the resonant effect of the cavity can be neglected and the emissivity approximated as a Lambertian emissivity of just the front mirror.

Thus, this arrangement essentially replicates the functionality of a conventional cold shielding used to restrict off-axis absorption and emission noise, but with much less hardware complexity . The maximum F number corresponding to the cavity acceptance angle is also shown in Fig. 2.2.

Using the piecewise approximation of equation 2.14 in equation 2.13 the photon noise due to incoming photons from the background is given by

$$\langle P_n^2 \rangle = \langle P_n^2 \rangle_{in} + \langle P_n^2 \rangle_{out} \tag{2.15a}$$

where

$$\langle P_n^2 \rangle_{in} = 16\pi \sin^2(\frac{\theta_{1/2}}{2}) h^2 c^3 A \int_{\lambda} \frac{\epsilon_{in}(\lambda)}{\lambda^6 (e^{hc/\lambda k_B T} - 1)} \left[1 + \frac{\epsilon_{in}(\lambda)}{e^{hc/\lambda k_B T} - 1} \right] d\lambda \tag{2.15b}$$

$$\langle P_n^2 \rangle_{out} = 4\pi \cos^2 \theta_{1/2} h^2 c^3 A \int_{\lambda} \frac{\epsilon_{out}(\lambda)}{\lambda^6 (e^{hc/\lambda k_B T} - 1)} \left[1 + \frac{\epsilon_{out}(\lambda)}{e^{hc/\lambda k_B T} - 1} \right] d\lambda \tag{2.15c}$$

The total noise power will be the quadrature sum of the power absorbed and the power radiated by the detector. In the ideal condition where electrical noise is completely absent the specific detectivity under background limited conditions is given by $D^* = [\langle P_n^2(T_{det}) \rangle + \langle P_n^2(T_{bkg}) \rangle]^{-1/2}$ where T_{det} and T_{bkg} are the detector and background temperatures respectively. Any electrical noise power if present, adds to this photon noise power and reduces the detectivity.

Fig. 2.3 shows the calculated photon noise limited detectivity for increasing cavity half width under an ideal photon noise limited condition and also under the presence of electrical noise. The dotted horizontal line indicates the noise for a broadband blackbody absorber. This noise level is considered as a fundamental performance limit for all thermal detectors. The numbers indicated in the legend are the electrical noise levels as a fraction of the blackbody photon noise.

With decreasing cavity resonance width the magnitude of the photon noise decreases and the detectivity increases. This is because of at narrow resonance widths the cavity acceptance angle $\theta_{1/2}$ progressively decreases to smaller values. The incident power contained inside this cavity half angle is then much lower than that outside of it. Consequently the photon noise is dominated by the photon noise outside the half angle $\langle P_n^2 \rangle_{out}$ as opposed to the noise inside

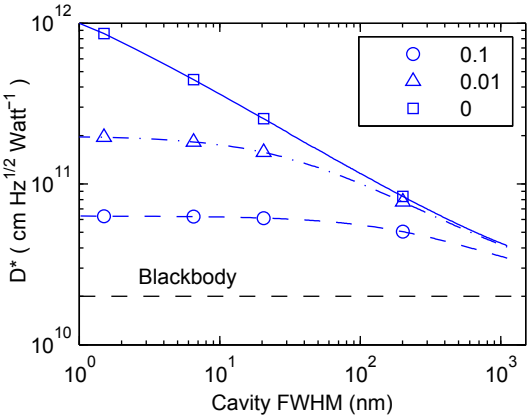

Figure 2.3: Detector D* for various values of electrical noise for various cavity half widths. The box shows the magnitude of the electrical noise NEP relative to the blackbody photon noise.

the half angle $\langle P_n^2 \rangle_{in}$. The quantity $\langle P_n^2 \rangle_{out}$ depends directly on the magnitude of the single pass emissivity of the front mirror membrane which is quite small for a narrow resonance width cavity. The total photon noise magnitude consequently decreases. In presence of electrical noise the D* levels off since the electrical noise is not affected by the cavity bandwidth.

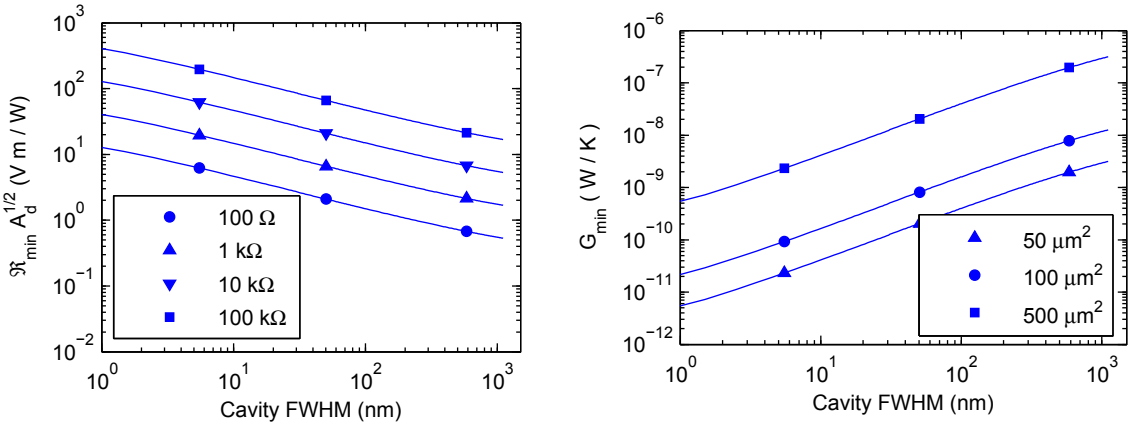

(a) (b)

Figure 2.4: (a) Minimum responsivity normalized to area for various detector resistances. (b) Minimum thermal conductance for various detector areas.

It is useful to determine the responsivity and the thermal conductance required to achieve photon noise limited performance. The electrical NEP per unit bandwidth for a purely Johnson

noise limited resistor is given by $NEP_e = \sqrt{4kTR_s}/\Re$ for a resistor of value R_s. Similarly the conductance NEP due to phonon fluctuations per unit bandwidth is given by $NEP_{TC} = \sqrt{4kT^2G}$ within the detector thermal bandwidth. Equating these to the photon noise of a cavity coupled absorber gives the minimum responsivity and the minimum thermal conductance for the respective NEPs be equal to the magnitude of the photon noise.

$$\Re_{min} = \sqrt{\frac{4k_BTR_s}{A_d\langle P_n^2\rangle}} \tag{2.16a}$$

$$G_{min} = \frac{\langle P_n^2\rangle A_d}{4k_BT^2} \tag{2.16b}$$

The minimum responsivity normalized to detector area and the minimum thermal conductance are plotted in Fig. 2.4a and Fig. 2.4b respectively for various cavity resonance widths. As an example, for a 100 nm wide cavity with 1 kΩ resistor and 100 μm^2 area, the electrical NEP equals the photon noise limited NEP for a responsivity $\Re_{min}$ of approximately 50,000 V/W. Similarly, at a thermal conductance of 10^{-9} W/K the thermal conductance NEP is equal to the photon NEP.

It can be seen that under a more general assumption of direction and wavelength dependent emissivity the background noise limit for a detector is lower than that of a broadband blackbody detector. This enhancement comes at the cost of a lower detector throughput $A\Omega$ and but would be useful when viewing spectrally narrow sources in presence of a hot background.

2.3 Passive detection of molecules

A cavity coupled detector limited by photon noise is ideally suited for measurement of narrow linewidth molecular spectra under the presence of hot thermal backgrounds. This measurement can be performed by utilizing radiation emitted by the thermal background without the need of any external illumination. A detection scheme using just the thermal brightness of the background as a radiation source is called passive standoff detection. Passive standoff detection for monitoring of gases has been under active development and instruments based on fourier transform and scanning Fabry-Perot interferometers have been demonstrated for this purpose

[30, 31]. For testing the performance of instruments SF_6 is a common molecule due to its strong absorption bands in the long wave infrared. In this section a radiometric model for calculating the signal from a molecular species at a distance is first described. It is then used to calculate the detection limits of SF_6 when observed with a background limited narrowband thermal detector.

2.3.1 Equation of transfer

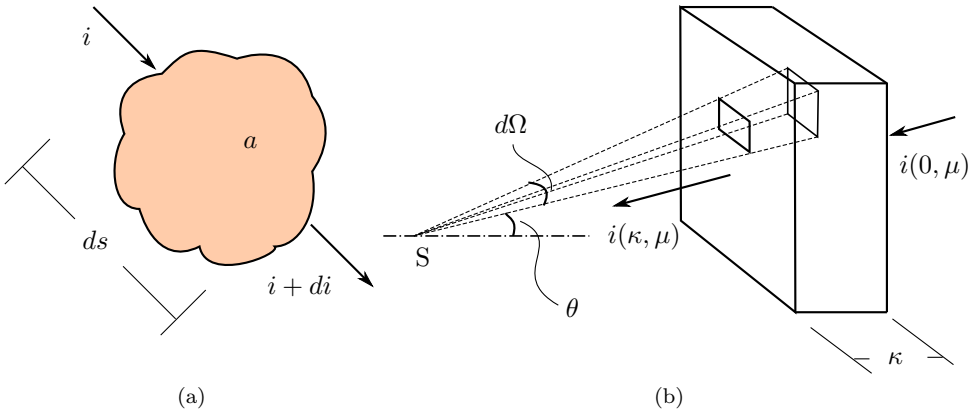

Figure 2.5: (a) A differential element of an absorbing non-scattering medium. (b)Diagram of a plane parallel medium showing the various differential quantities.

Radiation heat transfer calculations are conveniently performed on the basis of the radiant intensity i. This quantity which is the radiation energy per unit time per unit area per unit solid angle is an invariant in the absence of absorption, emission or scattering. In presence of these mechanisms, the radiant intensity has to be appropriately modified as described by the equation of transfer. Rigorous treatment of the equation of transfer has been given by several authors [32, 33, 34]. For long wave infrared radiation scattering by gaseous molecules can be assumed negligible which greatly simplifies the calculations.

The rate of change of intensity i with distance for a medium depends on the incident intensity and the extinction coefficient of the medium. For a differential element of length ds shown in figure 2.5a this is given by

$$di = -ai\ ds \tag{2.17}$$

where a is the wavelength dependent extinction coefficient. In presence of only absorption and self emission the differential form of the equation of transfer is given by

$$\frac{di}{d\kappa} + i = i_e \tag{2.18}$$

where $d\kappa = ads$ is the position dependent differential optical thickness and i_e is the intensity of self emission. The solution of this equation is given by

$$i(\kappa) = i(0)e^{-\kappa} + \int_0^{\kappa} i_e(\kappa^*)e^{\kappa^* - \kappa}d\kappa^* \tag{2.19}$$

where $i(0)$ is the incident intensity, κ^* is the dummy variable for integration of i_e along the entire path length. For thermal radiation, the quantity i_e is given by the radiant intensity $R_{bb}(T)$ at temperature T from Planck's law. The equation 2.19 can then be written as

$$i(\kappa) = i(0)e^{-\kappa} + R_{bb}(T)(1 - e^{\kappa}) \tag{2.20}$$

where $\kappa = \int ads$. The first term in the above equation gives the transmitted intensity through an absorbing medium analogous to Beer's law. The second term is just the Planck's radiant intensity multiplied by the medium emissivity given by $\epsilon_m = 1 - \exp(\kappa)$. For analyzing a finite sized object like a gas cloud, plane parallel geometry shown in figure 2.5b is frequently utilized. The radiant intensity traveling to the left at the exit face of the cloud can be after integrating the transfer equation can be written as (see [33])

$$i(\kappa, \mu) = i(0, \mu)e^{-\kappa/\mu} + R_{bb}(T)(1 - e^{\kappa/\mu}) \tag{2.21}$$

where $\mu = \cos(\theta)$ is the direction of radiation with respect to the normal to the plane and κ is the optical depth within the medium. This equation can be used to calculate the total intensity per unit time per unit area per unit solid angle at any point by simple summation of the intensities through each layer between the source and the observer.

As an example consider the system shown in figure 2.6. It consists of a detector with a

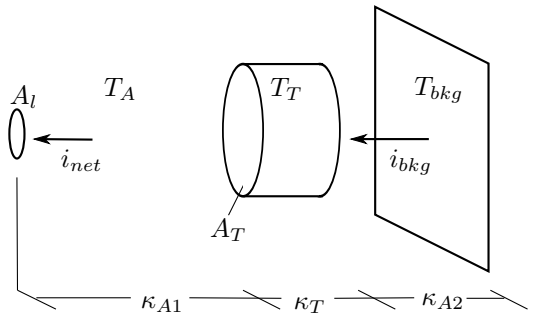

Figure 2.6: Layer structure for model used for passive standoff detection calculations.

collector lens area A_l viewing terrestrial background at temperature T_{bkg} through a cloud of gas. The plane parallel gas cloud has optical thickness κ_T and area A_T and is sandwiched by two plane parallel layers of atmosphere of optical depth κ_{A1} and κ_{A2}. After summing the intensities at the detector plane layer by layer, the net intensity at the plane of the lens is given by

$$\begin{aligned} i_{net}(\mu) = {} & R_{bb}(T_A)(1 - e^{-\kappa_{A1}/\mu}) + R_{bb}(T_T)(1 - e^{-\kappa_T/\mu})e^{-\kappa_{A1}/\mu} \\ & + R_{bb}(T_A)(1 - e^{-\kappa_{A2}/\mu})e^{\kappa_T/\mu}e^{\kappa_{A1}/\mu} + R_{bb}(T_{bkg})e^{-\kappa_{A2}/\mu}e^{-\kappa_T/\mu}e^{\kappa_{A1}/\mu} \end{aligned} \tag{2.22}$$

where T_A and T_T are the temperatures of the atmosphere and the target gas respectively. This equation can be rewritten more intuitively in terms of the emissivities ϵ and transmissivities τ of the various layers such that

$$\begin{aligned} i_{net}(\mu) = {} & R_{bb}(T_A)\epsilon_{A1} + R_{bb}(T_T)\epsilon_T\tau_{A1} \\ & + R_{bb}(T_A)\epsilon_{A2}\tau_T\tau_{A1} + R_{bb}(T_{bkg})\tau_{A2}\tau_T\tau_{A1} \end{aligned} \tag{2.23}$$

Thus the net intensity at the detector plane is thermal radiance from Planck's law multiplied by the emissivity of that layer and the transmissivity of every subsequent layer in the path to the detector. Similar layered models have been used previously in the literature [35, 36, 37]. A typical detection scheme will measure the incident spectrum both with and without the the target gas in the path. A subtraction of the two measurements gives the power absorbed or

emitted due to the target gas. The incident intensity from the background at the detector plane without any target gas in the path can be calculated for the system of figure 2.6 by

$$i_{bkg} = R_{bb}(T_{bkg})e^{-(\kappa_{A1}+\kappa_{At}+\kappa_{A2}/\mu)} + R_{bb}(T_A)(1 - e^{-(\kappa_{A1}+\kappa_{At}+\kappa_{A2})/\mu}) \tag{2.24}$$

where κ_{At} is the optical depth through the length of the original target gas but which is now occupied only by the atmosphere. The difference signal $\Delta i = i_{net} - i_{bkg}$ contains information about the characteristics of the target gas and can be integrated to obtain the net radiation signal measured at the detector from the difference of two measurements. The intensity difference is a function of the radiance contrast between the cloud and the background and depends on their respective temperatures and their emissivities. It is possible to have no radiance contrast between the target and the background in which case no signal can be detected.

The radiant flux q across all wavelengths and solid angles is given by integrating the radiant intensity across all wavelengths and solid angles. For a cavity coupled detector the intensity function has to be modified by the cavity absorption lineshape $f(\lambda)$. The power per unit area measured at the detector plane is then given by

$$q(\kappa) = \int_{\lambda} \int_{\Omega} \Delta i(\kappa, \mu) f(\lambda) \cos\theta \; d\Omega d\lambda \tag{2.25}$$

If the distance between the cloud and the detector is large, then the solid angle subtended by the cloud at the detector is small. Under this approximation the solid angle can be simplified such that $\int d\Omega = \pi A_T / L^2$ where A_T is the cloud area and L is the distance between the cloud and the collector lens. Under these simplifying assumptions the power measured by the detector is given by

$$P_d = \frac{\pi A_T A_l}{L^2} \int_{\lambda} \Delta i(\kappa, \mu) f(\lambda) d\lambda \tag{2.26}$$

The area of the collector optics A_l is of primary importance as seen from this equation. For coupling to a resonant optical cavity, it is sufficient to have a lens with a numerical aperture that matches the cavity acceptance angle, which is a relatively simple requirement. The actual size of the collector optic is determined by other constraints like aberrations and cost. These

system level requirements are not fundamental to the detector sensitivity analysis and will not be considered in the calculations.

2.3.2 Synthetic spectrum using HITRAN

In order to find the optical depth of a layer for use in equations 2.22 and 2.24 it is necessary to know the absorption coefficients at the wavelength of interest for each molecular species in the path. Such calculations can be performed using the HITRAN database of molecular spectra [38]. This database contains either the calculated line transition parameters for several molecules and directly tabulated infrared cross sections at different pressures and temperatures for some others. The synthetic spectra generated using HITRAN have been verified for accuracy by several authors [39, 40] and serves as the basis for high resolution atmospheric transfer codes like MODTRAN [41].

The optical depth κ_i for a gas at temperature T and pressure p and at frequency ν is given by

$$\kappa(\nu, T, p) = \alpha_i(\nu, T, p) C_v s \tag{2.27}$$

where α_i is the absorption cross section, C_v is the volume concentration (molecules/cm^3) and s is the path length (cm). If there are multiple species present in the path, the net optical depth at a particular frequency can be found by summation of the individual species.

$$\kappa(\nu, T, p) = \sum_i \kappa_i(\nu, T, p) \tag{2.28}$$

The absorption cross section is the product of line intensity S and the line shape function f

$$\alpha(\nu, T, p) = S_\eta(T) f(\nu, \nu_\eta, T, p) \tag{2.29}$$

where ν_η is the transition frequency for the transition η. The line intensity $S_\eta(T)$ depends on the population densities in the upper and lower states and is thus temperature dependent. At high pressure found in lower atmospheres, the lineshape is assumed to be Lorentzian. The lineshape

function is then given by

$$f(\nu, \nu_\eta, T, p) = \frac{1}{\pi} \frac{\gamma(p,T)}{\gamma(p,T)^2 + \{\nu - (\nu_\eta + \delta(p_{ref})p)\}^2} \tag{2.30}$$

where $\gamma(p,T)$ is the half line width of the transition , δ is a parameter that accounts for shift in transition frequency due to pressure and p_{ref} is the reference pressure assumed to be 1 atmosphere. The linewidth also needs to be corrected for pressure and temperature according to

$$\gamma(p,T) = (T_{ref}/T)^n \left[\gamma_{air}(p_{ref}, T_{ref})(p - p_m) + \gamma_{self}(p_{ref}, T_{ref})p_m\right] \tag{2.31}$$

where γ_{air} is the air broadened linewidth, γ_{self} is the self broadened linewidth, T_{ref} is assumed to be 296 K and p_m is the partial pressure of the gas given by $p_m = mp_{ref}$ where m is the mole fraction of the species. All the parameters required for the above calculations are tabulated in the HITRAN database. A free program JavaHAWKS (http://www.cfa.harvard.edu/hitran/welcometop.html) can be used to extract the parameters for a particular gas from the database for a range of wavelengths and then used in the above equations to obtained the absorption cross section α and the optical depth κ.

For some gases like SF_6 where the calculated parameters are not available, wavelength dependent absorption cross section α is tabulated for various pressures and temperatures. This data can be directly used in equation 2.27 to calculate the concentration dependent optical depth. The cross section data is tabulated for a range of wavenumbers and can be used to interpolate the cross section at an arbitrary wave number within this range. Example programs for calculating the absorption cross sections from line-by-line parameters (e.g. CO_2) and from tabulated data (e.g. SF_6) are given in the appendix.

2.3.3 Detection limits for SF_6

The equations given in the previous sections are used to calculate the detection limits for SF_6 with a cavity coupled narrowband detector. SF_6 has strong absorption bands around 10.55 μm and is commonly used for detection experiments in the 8-12 μm atmospheric window. The detection limit is determined by the received power at the detector and the detector NEP. The

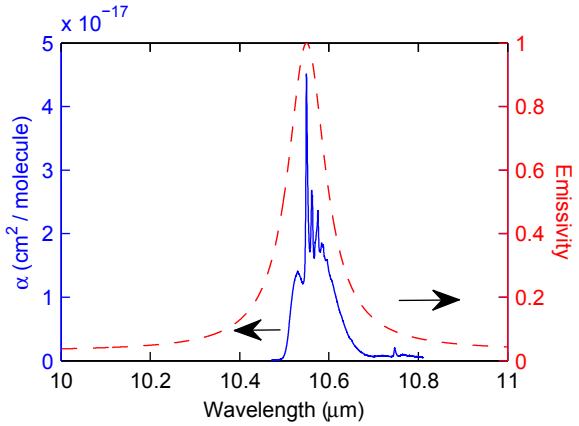

Figure 2.7: Absorption cross section of SF_6 (in blue) and cavity coupled detector emissivity (dashed red).

detector used for these calculations is chosen to have a front mirror reflectance R_1 of 0.94 and an emissivity of about 0.03. This detector has a FWHM of 105 nm, an acceptance half angle of 5.72° and photon noise limited detectivity of 1.1×10^{11} cm $\sqrt{Hz}$ Watt^{-1}. The choice of collector lens is somewhat arbitrary and is chosen to be 1 cm in diameter. It is also assumed that all of the power collected by the lens can be focused perfectly on the detector.

The detector is set up such that it views the cloud at normal incidence making $\mu = 1$. The atmosphere assumed to consist of 365 ppm of CO_2 and 100 ppm of H_2O. The SF_6 cloud is set to be 5 m diameter and 1 m in length and is sandwiched by 1 km of atmosphere on both sides. The background is assumed to be at 296 K and the cloud temperature is assumed to be equal to the atmosphere temperature. All these parameters can varied to examine their effect on the received power at the detector plane. An example MATLAB program that performs these computations can be found in the appendix.

Figure 2.7 shows the absorption cross section α of SF_6 which has a strong peak at 10.55μm. The emissivity of the detector centered at 10.55 μm is also shown in the figure. The pass band of the the detector is much larger than the absorption linewidth of SF_6.

The variation of the collected power with the concentration of SF_6 is shown in figure 2.8a and 2.8b for three different values of the cloud temperature. The background is held at 296 K for both plots, but its emissivity is set to 1 for figure 2.8a and 0.85 for figure 2.8b. The detector

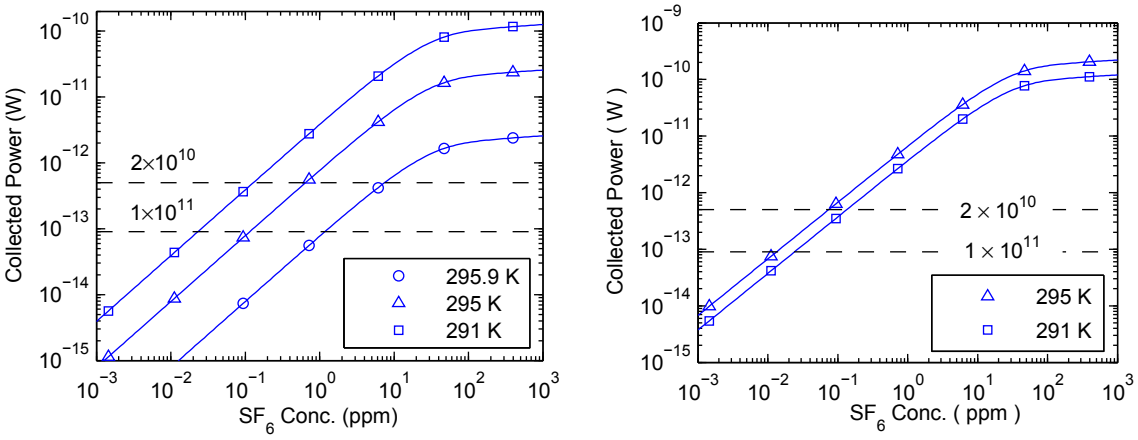

Figure 2.8: Power at detector vs. concentration for different cloud temperatures for background emissivity of (a) $\epsilon_{bkg} = 1$ and (b) $\epsilon_{bkg} = 0.85$. The background temperature is 296 K for both cases.

center wavelength is set at a constant value 10.55 μm for this simulation. The horizontal dashed lines show the NEP values for a 100 μm $\times$ 100 μm detector for two different detectivity values which represent the minimum detectable signal level.

The collected power is a function of the intensity difference Δi which is a function of the radiance contrast between the cloud and the background. The contrast increases with increasing temperature difference, thus generating a higher difference signal as seen in figure 2.8a. When the background emissivity is lower than 1 as in figure 2.8b it is possible to have a lower radiance contrast for a higher temperature difference leading to a net lower signal. This is because at an emissivity of 0.85, the radiance from the background is much lower and is closer to the radiance of the cloud at 291 K, thus reducing the difference signal. Hence the background can have a dramatic effect on the detection limits and it is important to have some information about the background temperature and its emissivity for extracting quantitative information from the measured spectra. (See [37] for detailed discussion on thermal radiance contrasts).

The radiance signal also increases with the concentration but saturates at high values when the cloud emissivity approaches unity. From figure 2.8a it can be seen that the for a 1 K temperature difference, the detection limit is 0.5 ppm for a 100 μm detector with D* of 2×10^{10}

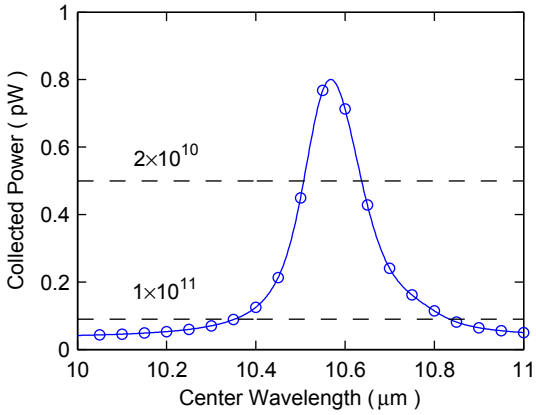

Figure 2.9: Power measured under scanning mode of operation for different center wavelengths corresponding of the cavity absorption spectrum. Circles indicate data in steps of 50 nm.

cm $\sqrt{Hz}$ Watt^{-1} and 0.01 ppm for a D* of $1{\times}10^{11}$ cm $\sqrt{Hz}$ Watt^{-1}. These concentration values correspond to an NEP of 1 and are optimistic estimates.

The cavity coupled detector can also be used in scanning mode across a range of wavelengths. Figure 2.9 shows the operation of the detector under this step scan mode when scanned from 10 to 11 μm. For this simulation, the SF_6 concentration is set at 1 ppm with a cloud temperature of 295 K. The solid curve is generated with a fine scan resolution. The solid curve is identical to that generated using convolution of the absorption spectrum and the filter absorption spectrum. The circles indicate the power measured if the detector mirror spacing was changed in discrete steps of 50 nm. For a detectivity of 2×10^{10} cm $\sqrt{Hz}$ Watt^{-1} only a few data points near the very peak of resonance will be detected. Where as with a detectivity of 1×10^{11} several data points lie above the detector noise limit.

Chapter 3

Resonant absorption in optical cavities

3.1 Analytical formulation

In this section the conditions for resonant absorption in optical cavities is derived analytically and it is shown that perfect absorption in ultra thin layers is possible. This is unlike the analysis of an absorbing Fabry-Perot cavity where the absorbing medium is uniformly distributed between the mirror elements. In this analysis field amplitudes are written in terms of the mirror properties instead of the Fresnel reflection and transmission coefficients at each interface. This enables us to analytically solve the resonance behavior of such systems without explicitly knowing the indices of refraction of the constituent materials, but is useful only when the number of components in the cavity is small. This method is based a multi-mirror Fabry-Perot analyis [42] but has been extended to include absorption in the mirrors. The optical cavity is shown in Figure 3.1 where each mirror is infinitesimaly thin and the i^{th} mirror has field reflectivity r_i, transmittance t_i and absorptivity a_i such that $r_i^2 + t_i^2 + a_i^2 = 1$. The thin absorbing mirrors are separated by distance l_i in vacuum. This configuration is different from the usual treatment where the absorption is distributed throughout the thickness of the slab. Following the notation of van de Stadt [42], we have

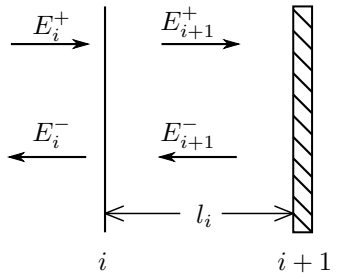

Figure 3.1: Schematic figure of the mirror system used in the analytical formulation.

$$E_{i+1}^+ exp(-i\phi_i) = t_i E_i^+ + r_i E_{i+1}^- exp(i\phi_i) \tag{3.1a}$$

$$E_i^- = -r_i E_i^+ + t_i E_{i+1}^- exp(+i\phi_i) \tag{3.1b}$$

where $\phi_i = 2\pi l_i/\lambda$ is the phase accumulated in a length l_i. Hence eliminating E_i^+ from the second equation and using $r_i^2 + t_i^2 = 1 - a_i^2$ we get

$$E_i^- = \frac{1}{t_i}\left[-r_i exp(-i\phi_i)E_{i+1}^+ + (1-a_i^2)exp(i\phi)E_{i+1}^-\right] \tag{3.2}$$

Writing these in matrix form we get

$$\begin{pmatrix} E_i^+ \\ E_i^- \end{pmatrix} = \frac{1}{t_i}\begin{bmatrix} e^{-i\phi_i} & -r_i e^{-i\phi_i} \\ -r_i e^{-i\phi_i} & (1-a^2)e^{i\phi_i} \end{bmatrix}\begin{pmatrix} E_{i+1}^+ \\ E_{i+1}^- \end{pmatrix} \tag{3.3}$$

or equivalently

$$E_i = M_i E_{i+1} \tag{3.4}$$

Note that there is no phase change is assumed upon reflection from a mirror. For n such mirrors in series,

$$E_1 = M_1 \times M_2 \ldots M_{n-1} \times E_n \tag{3.5a}$$

or

$$\begin{pmatrix} E_1^+ \\ E_1^- \end{pmatrix} = \frac{1}{t_1 t_2 \ldots t_{n-1}} \begin{bmatrix} A & B \\ C & D \end{bmatrix} \begin{pmatrix} E_n^+ \\ E_n^- \end{pmatrix} \tag{3.5b}$$

The field reflectance is given by

$$r = \frac{E_1^-}{E_1^+} \tag{3.6}$$

If the back mirror is completely reflecting as in a Gires-Tournois cavity, then $E_n^-/E_n^+ = 1$ and using equations 3.5a and 3.6 the reflectance can be written as

$$r = \frac{C + DE_n^-/E_n^+}{A + BE_n^-/E_n^+} = \frac{C + D}{A + B} \tag{3.7}$$

For perfect absorption at resonance the amplitude reflectance given by $R = rr^* = 0$ which can be solved to find conditions for coherent absorption. We shall now examine some properties of a two mirror cavity with completely reflecting back mirror and briefly discuss three mirror cavities.

3.1.1 Two mirror cavity

A two mirror cavity is the same shown in Figure 3.1 but with a completely reflecting back mirror. The front mirror has some field absorptivity a_1 and a completely reflective back mirror such that $r_2 = 1$. The intensity reflectivity in this case is given by

$$R = rr^* = \frac{r_1^2 + (1 - a_1^2)^2 - 2r_1(1 - a_1^2)\cos 2\phi}{1 + r_1^2 - 2r_1 \cos 2\phi} \tag{3.8}$$

Imposing the condition $R = 0$ for coherent absorption, we get the following conditions.

$$r_1 = (1 - a_1^2) \tag{3.9a}$$

$$\phi = m\pi; \quad m = 0, 1, 2... \tag{3.9b}$$

The first condition imposes a restriction on the absorptivity of the mirror to match its re-

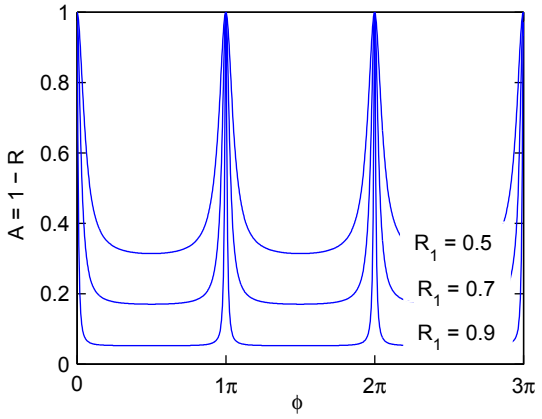

Figure 3.2: Coherent absorption with phase.

flectance. The second condition, which imposes a restriction on the mirror spacing, is not a general condition because this analysis does not account for phase change on reflection from the front mirror. If there is a strong phase change due to, for example a metallic mirror, then the phase matching condition from equation 3.9b will be different. A plot of absorption with phase is shown in figure 3.2 for different front mirror reflectivities $R_1 = r_1^2$ for a matching mirror absorption from equation 3.9a.

It can be seen that complete resonant absorption is obtained at cavity phase lengths given by condition 3.9b. Also note that even at off resonance, the absorption is never completely zero. This is because any incident field will travel through the top mirror at least once in which case there will be some absorption. Also the finesse of the absorption resonance increases with increasing mirror reflectivity analogous to a Fabry-Perot cavity because of the increasing field confinement as shown in 3.2.

3.1.2 Three mirror cavity

Analysis of a symmetric three mirror cavity with $\phi_1 = \phi_2 = \phi$ is analogous to a two mirror cavity. Here it is assumed that $r_3 = 1$ and the absorption is only present in the middle mirror ($a_1 = 0$).

The condition for perfect absorption at resonance is given by $R = rr^* = 0$. Using equation 3.3, 3.5a and 3.6 we get the condition for perfect absorption to be

$$a_2^2 = (1 - r_2)(1 + r_1) \tag{3.10a}$$

$$\phi = (m + 1/2)\pi; \quad m = 0, 1, 2... \tag{3.10b}$$

The phase condition once again corresponds to the middle mirror positioned at the field maxima which occurs when ϕ is an odd multiple of $\pi/2$. The second condition gives the restriction on middle mirror absorption. This condition is more constrained because now the absorption has to match the reflectance of both the front and the middle mirror.

3.2 Cavity Design in long wave infrared

In this section we will expand on the resonant absorption in two and three mirror cavities discussed in the last section and discuss the design of such cavities in the long wave infrared. The basic idea is to start with a thin film multi-layered cavity structure with a resonant air gap and then introduce controllable absorption in one of the layers to achieve coherent absorption. Such thin film stacks can be conveniently analyzed using the matrix method given by [43]. A fast, fully vectorized program was written for the cavity analysis in MATLAB and is included in the appendix. Using this program, a thin film stack can be quickly optimized.

The materials required for thin film design in the long wave infrared are usually non-standard materials which can be hard to deposit. Typical thin film designs will have alternating high and low index layers. Several semiconductors like germanium (n = 4) and tellurium (n = 4.6) have a high index of refraction and are nearly transparent provided the free carrier absorption is low. Several metal halides and oxides can be used for low index layers including sodium fluoride (n = 1.3) and barium fluoride (n = 1.5). Properties of several useful infrared thin films are

summarized in the literature [2, 44, 45].

3.2.1 Two mirror cavity designs

In section 3.1 conditions for perfect resonant absorption in two-mirror optical cavities were discussed. In this section we will discuss the practical design aspects of such cavities for use in thermal detector structures. During the course of this thesis two-mirror cavities were primarily explored. These cavities are easier to build because only one cavity spacing needs to be controlled, as opposed to three mirror cavities where two cavity spacings need to be optimized. The disadvantage of two mirror cavities is that it is more difficult to get high finesse and sharp resonances.

A two mirror resonant absorption cavity is essentially a Fabry-Perot cavity with absorbing mirrors. The absorption can be either in the front mirror (incident side) or the back mirror (non-incident side) and the thin film design is mostly similar for both configurations. The absorption in mirrors can be obtained using thin metallic films or free carrier absorption in doped semiconductors. In practice precise semiconductor doping is difficult because it requires ion implantation. Simple thermal implantation of germanium with antimony was briefly attempted during this project but was abandoned because high temperatures ($\geq$ 650 °C) were required to activate the antimony dopants.

Two mirror cavity - absorbing front mirror

Table 3.1 shows a basic layer structure for a two mirror cavity with an absorbing front mirror and a completely reflecting back mirror. The top mirror is germanium with thin film of nickel to obtain absorption. The width of the resonance depends significantly to the thickness of the germanium since that determines the top mirror reflectivity. Figure 3.3a shows the simulated reflectance from a two level cavity of Table 3.1 and its dependence on the germanium thickness. The dispersion in nickel is modeled using coefficients from a Drude model from Rakic [1]. It can be seen that the FWHM of the resonance decreases with increasing germanium thickness, varying from around 1.30 μm at for a 300 nm germanium layer to 580 nm for a 560 nm germanium layer. Even though it is desirable to have thicker germanium films and narrow resonances, the design

Layer	Thickness (nm)	n	k
Al_2O_3	20	1.3	0
Ni	3	7.33	33.13
Ge	300	4	0
Al_2O_3	20	1.3	0
Air	$\lambda/2$	1	0
Ge	$\lambda/4n$	4	0
NaF	$\lambda/4n$	1.3	0
Ge	$\lambda/4n$	4	0
NaF	$\lambda/4n$	1.3	0
Si	substrate	3.42	0

Table 3.1: Layer structure for front mirror absorption cavity. n and k for Ni are given at $\lambda = 9\mu$m using Drude model [1].

time constant of the thermal detector would set an upper limit on the germanium thickness. Also, note that the resonance position is not exactly at 10 μm (2*cavity spacing) as would be expected analytically and is due to significant phase shift upon reflection introduced by the top mirror.

It is also possible to get narrower resonance with thinner germanium layer if the cavity spacing is increased. This is shown in Figure 3.3b which shows the absorption in the optical cavity of Table 3.1 for a 300 nm germanium layer with a 5 μm and a 10 μm mirror spacing. The FWHM of the 10 μm cavity is now 1.07 μm as compared to the 1.30 μm width for a 5 μm mirror spacing. The finesse of this cavity is unchanged, however, and the improvement is only because the resonant absorption is now through a higher order mode. This also has the disadvantage of having multiple resonances occurring in the area of interest like the resonance at 6.7 μm in the Figure 3.3b.

Two mirror cavity - absorbing back mirror

An alternative configuration for a two mirror cavity is using an absorbing back mirror. In this design a thick metallic film is used as a back reflector and its low single pass absorption is amplified inside an optical cavity. Since a thick metallic film typically has low absorption it needs to be coupled to a high finesse cavity to achieve significant absorption. One such configuration is described in Table 3.2 where a thick nickel film acts as a back reflector and absorber when coupled to high reflectivity top mirror.

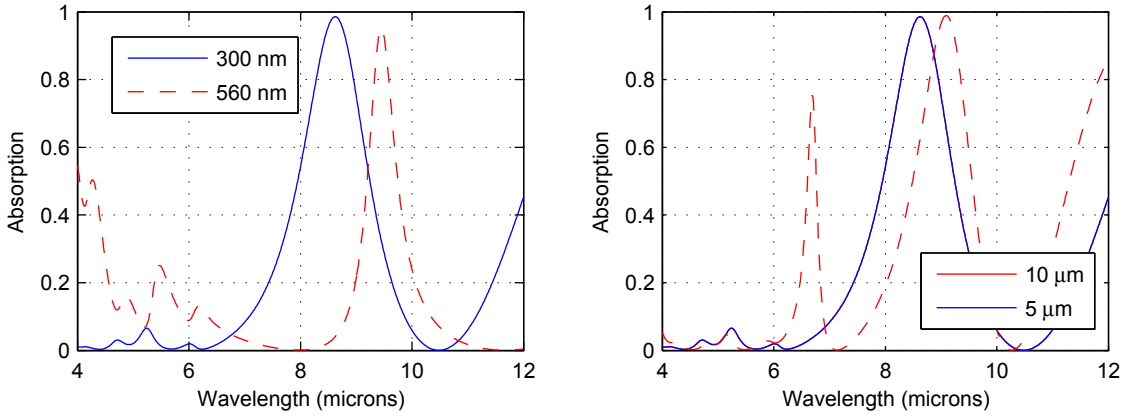

(a) (b)

Figure 3.3: Absorption for cavity structure shown in table 3.1 for (a) different thicknesses of germanium (b) different air gaps for a 300 nm germanium layer.

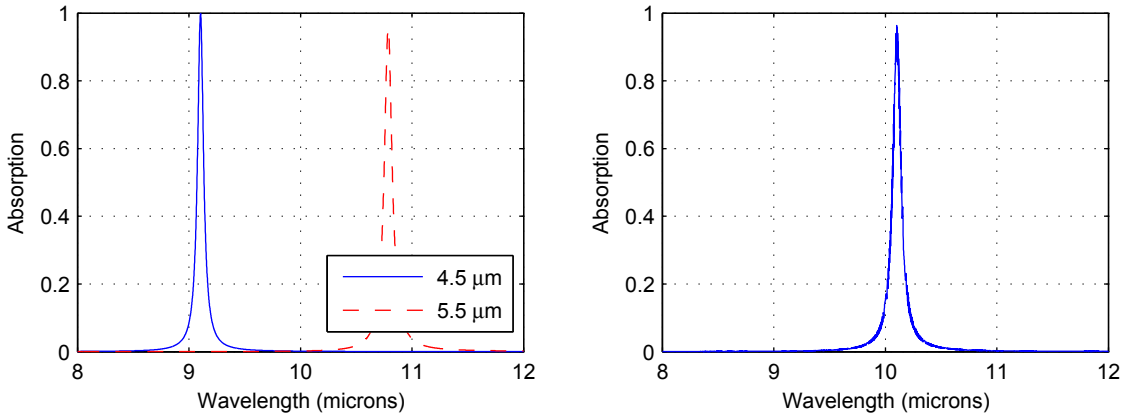

(a) (b)

Figure 3.4: Absorption for back absorbing mirror cavity structure shown in table 3.2 for (a) different cavity spacing (b) front mirror deposited on an AR coated NaCl substrate (n = 1.5) with 1 mm thickness.

Layer	Thickness (nm)	n	k
Air	incidence	1	0
Ge	$\lambda/4n$	4	0
NaF	$\lambda/4n$	1.3	0
Ge	$\lambda/4n$	4	0
Air	$\lambda/2$	1	0
Al_2O_3	20	1.3	0
Ni	150	7.33	33.13
Al_2O_3	20	1.3	0
Air	exit	1	0

Table 3.2: Layer structure for a back absorbing mirror configuration. n and k for nickel are given at 9 μm from a Drude model.

The absorption spectrum of this cavity is shown in figure 3.4a for two different air gaps. It can be seen that a very narrow resonances can be obtained due to the high finesse of this cavity. Another advantage of this configuration is that due to the use of a thick metallic film, the indices of refraction are expected to be consistent with values reported in the literature and will not depend strongly on the deposition conditions and film thickness. The top mirror in this configuration need not be a free standing membrane but could also be deposited on a low index substrate. Figure 3.4b also shows the absorption obtained for configuration in table 3.2 with the top mirror deposited on one side of a sodium chloride substrate (n = 1.5) with a sodium fluoride (n = 1.3) anti-reflective coating deposited on the other side. The absorption shows the effects of multiple passes inside the substrate which can be further minimized with a more complex A-R coating design. The disadvantage of this design is that it is harder to integrate in a dynamically tunable array.

3.2.2 Resonant cavity fabrication

This section discusses several aspects of fabrication and measurement for resonant absorption cavities. The cavities fabricated in the course of this thesis are of absorbing front mirror configuration. The cavities in this project are designed for use in high sensitivity thermal detectors and have to be integrated with an electrical readout scheme. A two wafer process was designed for this purpose because it provides more flexibility in designing the thermal conductance of the support structures. Such resonant absorption structures were previously investigated for

tunable absorption filters and were fabricated using a monolithic single wafer process [15]. The next sections give the details of (a) the methods of introducing controllable absorption in cavity mirrors (b) fabrication of Distributed Bragg Reflectors (DBR) in the long wave infrared (c) multi-wafer process for cavity fabrication (d) methods of cavity assembly.

3.2.3 Absorption in metals

Two common ways of introducing optical absorption in optical cavities are using a thin metallic film or using a doped semiconductor as a cavity element. Many metals have a large optical constant ($\tilde{n} = n + ik$) in the IR and thick metallic films strongly reflect the incident radiation. Ultra-thin metal films ($\leq$ 10nm) are required if higher absorption is desired. Due to their high index, metallic films also introduce a strong phase change on the incident radiation.

The refractive index of metallic films varies with the deposition conditions and the film thickness. It is common practice approximate $n = k = (\sigma/2\omega\epsilon_0)^{1/2}$ in the infrared where σ is the conductivity, ω is the frequency and ϵ_0 is the permittivity of free space [46, 47]. This approximation is not valid for many metals in the 8-12 μm range. Refractive index values from standard handbooks should only be taken as a rough guideline since they are frequently compiled from bulk measurements [2]. The refractive index of several metallic films can been fit to a Lorentz-Drude model and the fit coefficients for several common metals has been given by Rakic [1]. However since the refractive index of thin metallic films is thickness dependent, it is better if it is directly measured in the region of interest for a particular film thickness and a particular deposition condition.

Several methods have been discussed in the literature for measuring optical constants of thin metal films. These include inversion of reflection and transmission measurements [48], Kramers-Kronig analysis [49] and ellipsometry [50]. A Fourier Transform Infrared (FTIR) system is a commonly available instrument and can be used to perform reflection and transmission measurements in the infrared. A method of determining optical constants of metallic films using an FTIR system is discussed in the next section.

Measurement of Optical Constants using FTIR

The metallic thin films to be measured are deposited on ultra-thin ($\sim$ 10nm) free standing films of ALD Al_2O_3. These free standing films are deposited on a thin silicon wafer and etch released using a DRIE Bosch process. The reflectance (R) and transmission (T) of these metallic films are next measured with an FTIR microscope. The thickness of the thin film is independently measured using a visible wavelength spectroscopic ellipsometer since this would be invariant across wavelengths. This thickness can then be used to invert the R and T using the method described by Nestell and Christie [51] to obtain the refractive index components n and k of the film.

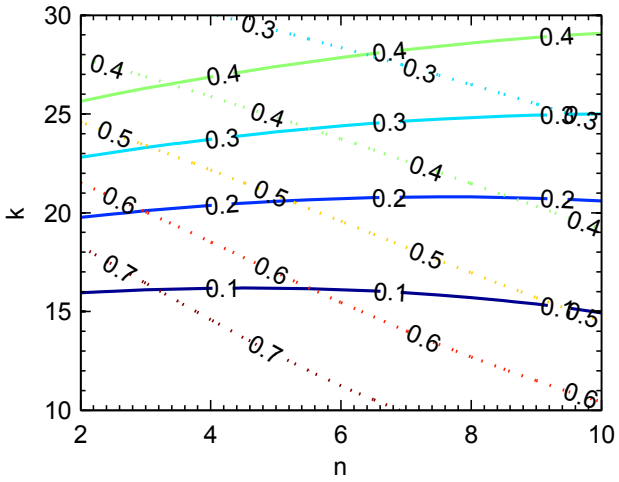

Figure 3.5: Contour plot of reflectance and transmission of a 4 nm thick film at 9 micron wavelength.

This method involves finding the intersection of the measured R and T values on the n-k plane for each wavelength that the R and T are measured at. A contour plot of R and T for a film with thickness d = 40 μm at 9 μm wavelength is shown in Figure 3.5. The reflectance is plotted as solid while the transmission is plotted as dotted line. For example, a measured R value of 0.2 and T of 0.5 the n and k can be read off the chart as 5.2 and 21 respectively.

It important to remember that while the reflected and transmitted intensity R and T are single valued functions of refractive index n and extinction coefficient k, the reverse is not true.

Multiple values of n and k can give same values of R and T. In case of metallic thin films in the long wave IR these points of intersection are well separated. However in case an ambiguity arises due to multiple intersections then additional information is needed to correctly identify the intersection point. Also, since it is extremely tedious to graphically find the n and k for large number of wavelengths, a numerical method can be implemented to perform this computation [51].

The major advantage of depositing metallic films on thin free standing membranes is that substrate effects are now negligible. It can be shown in a straightforward manner that if the optical thickness of the Al_2O_3 film is small then the R and T are only affected by the metallic film. Thus a knowledge of the Al_2O_3 refractive index is not required while inverting the measured R and T. Additionally, compared to a thick substrate, there are no resonance effects due to multiple passes of the light within the substrate. With a thick substrate it can be challenging to decouple these resonance effects with the effect of the metallic film on the reflectance and the transmittance.

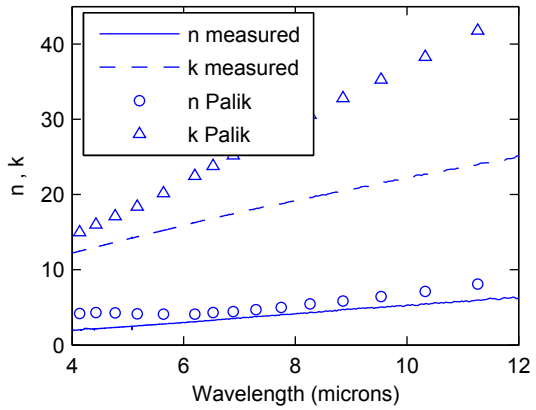

Figure 3.6: Refractive index for thin sputtered Ni film on Al_2O_3 membranes calculated from R-T data from FTIR microscope (n - solid, k - dashed lines). Also shown is data from Palik [2] (n - circle, k - triangles).

The optical constants of several metals like Pd, Au and Ni were measured using this method. As expected, the optical constants varied with film thickness. Figure 3.6 shows the optical constants obtained by R-T inversion for a sputtered Ni film on 10 nm Al_2O_3 free standing film. The Ni film is DC sputtered for 40 seconds at a substrate temperature of 180 °C and

has a thickness of 4 nm as measured by a spectroscopic ellipsometer. It can be seen that the general shape of the dispersion curve is same as the literature data but the actual magnitudes are lower. The extinction coefficient is expected to vary with film thickness and packing fraction as expected from the Maxwell-Garnett theory [52].

Nickel was found to have the most consistent values for optical constants and was thus chosen for use in the optical cavities. Ni is a high melting solid and there is good agreement in the literature on its infrared optical constants. Other metals like Pd and Au were found to were measured to have anomalously low extinction coefficients in the 8-12 μm range.

3.2.4 Bragg Reflectors

High reflectivity non absorbing Bragg mirrors can be fabricated by depositing alternating low index and high index layers of quarter wave optical thickness. Semiconductors like germanium and tellurium can be used as high index layers. Low index materials include metal halides like sodium fluoride, metal oxides, zinc sulfide and zinc selenide. With a high index contrast stack like germanium (n = 4) and sodium fluoride (k = 1.3) a high reflectivity DBR is achievable with as few as 2 pairs on Silicon. However the thickness of each individual layer is high and careful stress control is required to grow a mechanically stable stack. If a little amount of absorption is acceptable then a hybrid dielectric-metal reflector can also be used for optical cavities. Bare metallic film have some surface absorption which can be amplified inside a cavity due to multiple passes. By depositing a dielectric on top of this metal, a high reflectivity and reduced absorption can be obtained by using less number of dielectric pairs than a full Bragg stack.

Several Bragg mirror stack were grown during the course of this project. All the layers are deposited in a thermal evaporator. Some materials like zinc sulfide require the use of a specialized boat obtained from R.D. Mathis company for an evaporation source. These boats hold large quantity of material and have radiation shields for uniform heating. Substrate temperature control is required for depositing the layers since substrate temperature control has big effect on the layer stress and surface roughness. The thickness of the film is monitored using a quartz crystal. A calibration run is usually required first to determine proportionality factor between the quartz crystal reading and the actual film thickness on the wafer.

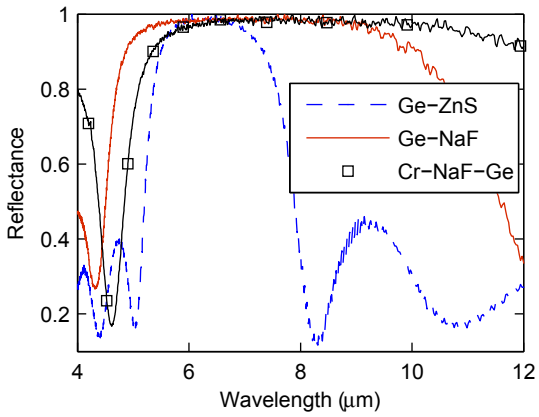

Figure 3.7: Normalized FTIR reflectance of DBR stacks in the infrared for three thin film material combinations - 8 layer Ge-ZnS, 4 layer Ge-NaF and hybrid Cr-NaF-Ge.

Figure 3.7 shows the measured reflectivity using an FTIR of an eight layer Ge-ZnS stack, a four layer Ge-NaF stack and three layer Cr-NaF-Ge stack. High reflectivity is obtained in each of these cases. The DBR passband depends on the index contrast between the high and the low index layers and thus a Ge-ZnS has a smaller reflectance band than Ge-NaF or Cr-NaF-Ge stacks. The choice of a particular material system is based primarily on the experimental difficulty in depositing the individual layers. Germanium with its higher melting point is a difficult material to evaporate in large quantities in a thermal evaporation system. But germanium films have low surface roughness and can adhere well to heated substrates. Tellurium is a low melting material and evaporates easily but the resulting films have poor surface roughness at elevated substrate temperatures. Sodium fluoride has a low index of refraction but high tensile stress which makes thick quarter wave layers susceptible to delamination. Zinc sulfide has low compressive stress when deposited on heated substrates but due to its higher index (n = 2.2) more layers and time are required for full DBR stack. Thus there is an engineering tradeoff in every material system that was investigated.

The best thin film combination that could be produced with reasonable ease was germanium and sodium fluoride 4 layer stack. The big disadvantage of this stack was its gradual delamination with time. For low finesse cavities a hybrid Cr-NaF-Ge stack was found to be sufficient reflectance and better stability than a 4 layer stack. This hybrid stack is evaporated

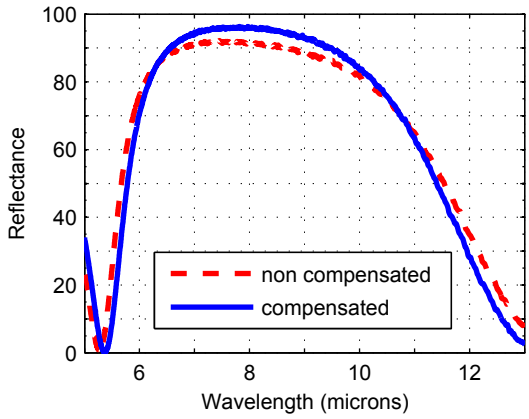

Figure 3.8: FTIR reflectance from 3 layer Ge-Zns-Ge DBR membrane with air as both incident and exit medium. Blue shows non-quarter wave stress compensated membrane. Red shows near quarter wave membrane without any stress compensation.

in a single run in a thermal evaporation chamber and the substrate is held at 180 °C for the entire deposition. Chromium is evaporated using evaporation sticks, germanium is evaporated using a simple open tungsten boat and sodium fluoride is evaporated using a baffled box source (R.D. Mathis company SB-10).

High reflectance can also be obtained with free standing multi-layered membranes. Since these membranes are bounded by air on both sides, higher reflectivity can be obtained compared to the same stack deposited on Silicon. Such mirror membranes can be useful as top mirrors in three level cavities and in tunable filters. Three layer Ge-ZnS-Ge membranes were fabricated using thermal evaporation and DRIE etch release. Good stress compensation is required to achieve flat membranes after etch release. While a quarter wave thickness gives the best possible reflectivity for a given wavelength, it is possible to achieve good reflectivity with a non-quarter wave stack. A non-quarter wave design is useful for multilayer membranes because the thickness of individual layers can be modified to get better stress compensation. Figure 3.8 shows the FTIR reflectance data from a non-stress compensated near quarter wave mirror membrane and a stress compensated non-quarter wave membrane. Since the incidence and exit medium is air in both cases high reflectance is obtained with just three layers in both cases. The mirror curvature is dramatically different due to better stress compensation in the non-quarter wave case.

Initially, the layers were deposited on substrates heated at 200 °C with thicknesses close to a

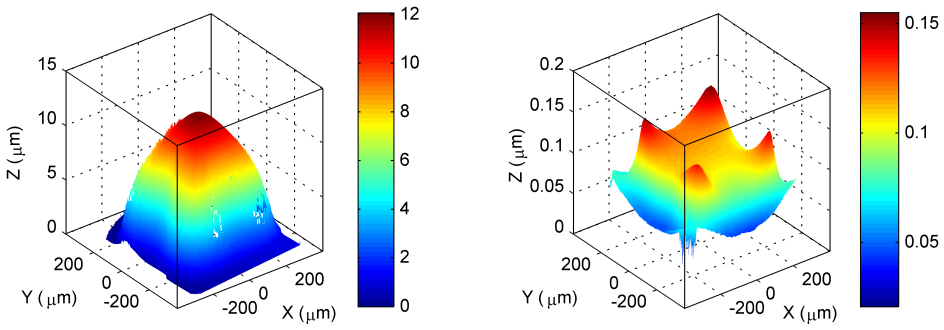

(a) (b)

Figure 3.9: Interferometric surface profile for a 3 layer DBR membrane for (a) no stress compensation (b) stress compensation. Color bar shows vertical deflection in microns.

quarter wave. The resulting structure had high compressive stress and hence buckled after etch release. Figure 3.9(a) shows the interferometric image of a buckled membrane with a radius of curvature 2.83 mm. To obtain flat structures, the two germanium layers were deposited at substrate temperature of 40 °C to maximize the tensile stress, while the ZnS was deposited at 200 °C to reduce its compressive stress. Additionally, the ZnS thickness was reduced and the Ge thickness increased from the ideal quarter wave thickness. The final structure showed good flatness after etch release as shown in figure 3.9(a) with a radius of curvature is 2.62 meters. Figure 3.10 shows the effect of substrate temperature on the stress of various infrared transparent thin films. It can be seen that substrate temperature can be used to effectively control the stress in these films, especially zinc sulfide.

3.2.5 Optical cavity fabrication process flow

The basic process flow for fabricating these two wafer optical cavities similar to the detector fabrication process that will be discussed in chapter 4. The layer structure is similar to that shown in Table 3.1. The top wafer is first coated with $\sim$ 22 nm of ALD Al_2O_3. The top mirror and absorber consists of a germanium layer ($\sim$ 300 nm) with a thin film of nickel ($\sim$ 3nm). These are deposited using DC sputtering at 250 °C substrate temperature. Sputtering is preferred over e-beam evaporation because evaporated germanium films have poor adhesion.

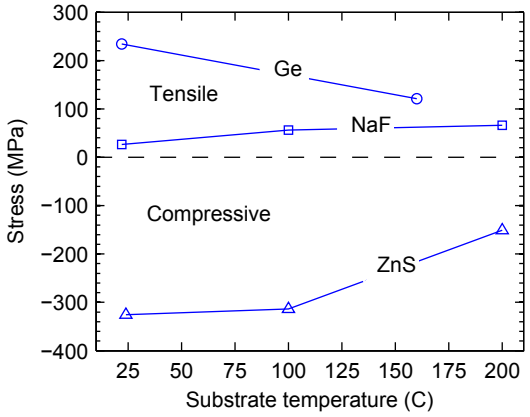

Figure 3.10: Stress variation of thermally evaporated thin films with substrate temperature.

These layers are then coated with ALD Al_2O_3 which is patterned in BCl_3 plasma. The back side of the wafer is coated with e-beam evaporated Al_2O_3 which functions a hard mask for etching. The backside Al_2O_3 is patterned with a Buffered Oxide Etch (BOE). The top wafer is then etched in Deep Reactive Ion Etching (DRIE) which etches through the silicon wafer and stops on the Al_2O_3 on the front side to release the top mirror structures. Figure 3.11 shows a released top mirror membrane and its interferometric surface profile which shows that the device are finesse sufficient.

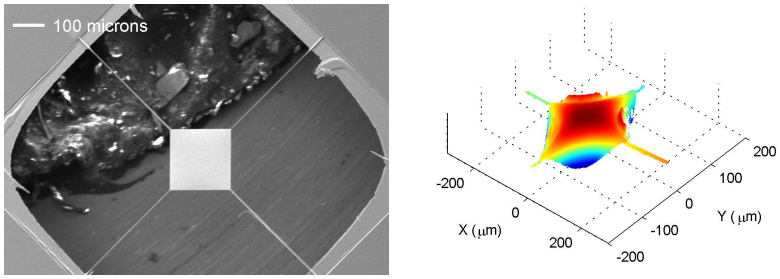

(a) (b)

Figure 3.11: (a)SEM image of an etch released Ge-Ni top mirror (b) and its interferometric surface profile.

Back mirror fabrication process

The back mirror is a DBR deposited on vertical pillars etched in silicon using DRIE. These pillars are etched in the device layer of an SOI wafer so that the DRIE can stop on the buried oxide layer. This ensures that the etched surfaces of the pillar wafer are smooth. To ensure that the pillar heights are as close to the top mirror thickness as possible, the SOI wafer is fabricated in-house using a fusion bonding process. In this process the bottom handle wafer is a standard thick silicon wafer while the top wafer is a thin double side polished wafer from the same wafer batch as the top mirror wafer. The thin double side polished wafers from the same wafer batch are specified within a thickness tolerance of ± X %.

The fusion bonding is performed in a wafer bonding system. Both handle and device wafers are first oxidized using wet oxidation process at 1150 °C. The wafers are then immersed in a solution of H_2SO_4:H_2O_2 at 100 °C to render the surface hydrophillic and increase the number of dangling -OH bonds on the surface The thin wafer is aligned with the thick wafer with thin wafer at the bottom. Bonding is carried out under pressure and 450 °C and forms a weak bond between the two wafers. The joined wafers are then annealed at 1150 °C for 4 hours to fuse the wafers together and form a strong bond. The wafers can be inspected with an infrared camera to determine the quality of the bond. It is important to keep wafer surfaces free of particles because presence of particulates between the wafers lead to voids. Figure 3.12 shows an IR photograph of a fusion bonded wafer. The dark regions show regions with voids and weak bonding.

If good particulate control is maintained then very good quality SOI wafers can be obtained with this process. During the bonding there were significant problems with surface quality of the device wafer after bonding due to particles from the bonder chuck. These particles on the wafer surface are impossible to remove after the 1150 ° anneal. Large areas of the bonded wafer were discarded due to the surface roughness introduced by these particles. The thickness of the pillars can be fine-tuned by etching further into the handle wafer of the SOI layer. DBRs are finally deposited on these pillars using thermal evaporation as described in the previous sections.

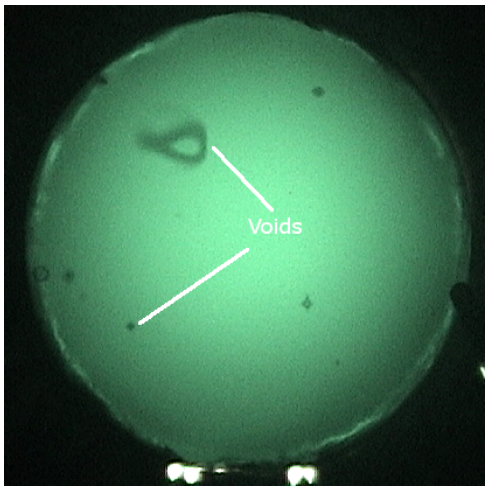

Figure 3.12: Infrared image of a fusion bonded wafer showing voids.

Cavity assembly

The final cavity is assembled by bringing the top mirror wafer and the bottom mirror wafer in close proximity with controllable separation, which can be a challenging task. Several methods were tried for cavity assembly. The most successful method was using a flip-chip bonding system to align the top and bottom mirror dies and bonding them together. The flip-chip bonder system can apply controllable pressure and temperature cycles to the clamped dies to achieve bonding.

Two types of bonding methods were found useful. The first method uses a metal solder foil as a spacer and bonding layer. The foil used for bonding is a eutectic alloy of 97% indium and 3% silver (Indium Corporation IndAlloy 290) with a melting point of 143 °C. Small pieces of foil are cut and put on the edges of the bottom die. The temperature is then ramped up to the melting point of the solder. The top die is then aligned and clamped with the hot bottom die. The amount of force applied during clamping determines the spacing obtained between the two dies. The dies are then allowed to cool down to at least 80 °C and removed carefully. This process forms a weak bond between the dies because the solder does not have good adhesion to the substrates. This method has a disadvantage that a heating cycle is required to achieve a bond. The heat cycling can be detrimental to thick DBR layers and can cause delamination.

The second method uses room temperature curing epoxy for bonding (Thorlabs F120). The basic method is the same as the metal foil except that no heating is required. This makes

the epoxy bonding method more compatible with temperature sensitive materials. Very small quantities of epoxy are applied to the corners of the bottom die before clamping. The bond is allowed to cure for at least 90 minutes before removing the dies, though it may require up to 24 hours to set completely. The spacing between the two dies is again determined by the clamping force. Very strong bonds are obtained with this method. A major disadvantage of an epoxy is that due to its viscous nature the dies frequently get misaligned during clamping.

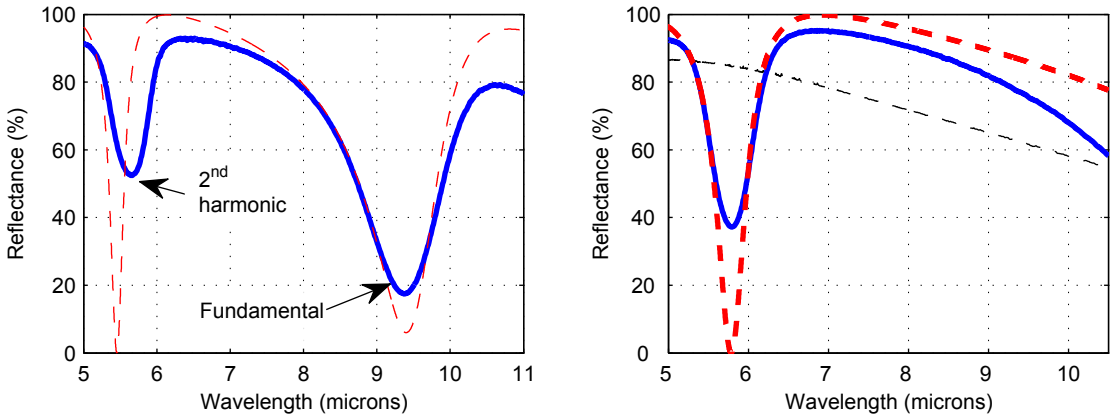

Figure 3.13: FTIR reflectance data for assembled cavities with two different spacings (a) 5.45 μm (b) 2.95 μm showing measurement (blue) and simulation (red).

The spacing between the mirrors can be confirmed using a confocal microscope. Resonance absorption from a cavity can be confirmed by measuring the reflectance spectrum from the top germanium mirror in an FTIR microscope. Figure 3.13 shows the reflectance spectrum of a cavity with two different spacings. These cavities were assembled by simple mechanical clamping of the two dies without using any bonding materials. The top mirror is germanium (300 nm) and nickel (3.5 nm) and the bottom mirror is a four layer tellurium-sodium fluoride DBR.

In Fig. 3.13a the spacing is adjusted to excite two absorption resonances a fundamental mode at 9.38 μm (FWHM = 1.16 μm) and the 2nd harmonic in the mid wave at 5.66 μm (FWHM = 0.53 μm). A different spacing, can give just a single mode resonance in the mid infrared (FWHM = 0.57 μm) as shown in Fig. 3.13b. Thus the mode of operation of the detector can be selected between dual band and single band by varying the air gap. A plane

wave multilayer simulation for the cavity is also plotted (in red) and is in good agreement with the measured data in terms of the peak position. The intensity of the measured reflectance peak is lower than the simulated, indicating less than 100% absorption. This indicates some loss in the cavity, a possible source of which could be scattering in the back mirror.

A few other methods were tried for cavity assembly with mixed success. These include eutectic bonding using evaporated and lithographically patterned thin films stack of tin and gold [53], thin double sided tape (Nitto-Denko #5600 5μm thickness) and custom built piezo-actuated z-axis stage. In the tin-gold thin film stack it is difficult to obtain the correct composition for the desired phase. The thin double sided tape, while a very attractive method due to its apparent simplicity, is difficult in practice because it is very challenging to apply the tape in a uniform layer. The piezo actuated stage custom stage was designed poorly and lacked the ability to align and hold dies close together. Die bonding using room temperature curing epoxy was found to be the most repeatable and reliable method for cavity assembly.

Chapter 4

Design, Fabrication and Characterization of Spectrally Selective Thermal Detectors

In this chapter design, fabrication and characterization of spectrally selective high detectivity thermal detectors will be discussed in detail. With these detectors a peak detectivity of at least 3×10^9 cm $\sqrt{Hz}$/Watt at room temperature has been realized using a low thermal conductance support structure and a low noise thermoelectric readout scheme. The detector is also integrated with an optical cavity structure to achieve high absorption at a specific wavelength. This detector has amongst the highest reported performance for room temperature detectors [7, 54, 55] in the long-wave infrared. These detectors are a significant step towards an ultimate goal of achieving room temperature detectors with narrowband detectivities approaching the background photon noise limit [56]

The first section describes general aspects of thermal detector design and some of the trade-offs that need to be considered when designing detectors. The second section describes the fabrication of these detectors in some detail, some parts of which have been covered in chapter 3. In the third section, measurement setups for optical and electrical characterization of these

detectors are described and the results are discussed in detail. Significant parts of the work described in this chapter, especially the thermoelectric detector fabrication, was performed by Ryan Shea.

4.1 Thermal detector design with thermoelectrics

The general design aspects of thermal detectors has been covered in detail previously [57, 58] . This work uses Seebeck effect in thin films for electrical readout and this section will focus primarily on detector design using thermoelectric thin films. The responsivity of a thermal detector is the ratio of voltage output to the power input. For a thermoelectric readout the detector responsivity to a sinusoidally modulated input at angular frequency ω is given by

$$\Re(\omega) = \frac{\Delta V_{out}}{\Delta P_{in}} = \frac{\epsilon(\lambda) N(\alpha_n - \alpha_p)}{G\sqrt{1+\omega^2\tau^2}} \tag{4.1}$$

where $\epsilon(\lambda)$ is the wavelength dependent emissivity, N is the number of thermocouple junctions, α_n and α_p are the Seebeck coefficients of the constituent materials, G is the total thermal conductance including radiation and $\tau = C/G$ is the thermal time constant. The specific detectivity of the detector is its Noise Equivalent Power (NEP) normalized to detector area and electrical bandwidth.

$$D^* = \frac{\sqrt{A_d \Delta f}}{NEP} \tag{4.2}$$

The net Noise Equivalent Power(NEP) of a thermal detector can be written sum of NEPs of several sources which are uncorrelated [59]. These NEPs are those due to thermal fluctuation noise NEP_{TC}, due to Johnson noise NEP_J and due to 1/f excess noise, $\mathrm{NEP}_{1/f}$ such that

$$\begin{aligned} NEP^2 &= NEP_{TC}^2 + NEP_J^2 + NEP_{1/f}^2 \\ &= G^2 \frac{k_B T^2}{C} + \frac{1}{\Re^2}\left[4k_B T R \Delta f + \kappa V_b^2 ln(\frac{f_2}{f_1})\right] \end{aligned} \tag{4.3a}$$

where $G = G_{rad} + G_{cond}$ is the net thermal conductance including due to radiation, C is the heat capacity, T is the temperature, k_B is the Boltzmann constant, R is the device resistance, Δ f is the measurement bandwidth, f_2 and f_1 are the upper and lower measurement frequencies

and V_b is the bias voltage. For a detector dominated by Johnson noise the detectivity reduces to

$$D^* = \frac{\Re\sqrt{A_d}}{\sqrt{4k_BTR}} \tag{4.4}$$

A thermoelectric readout scheme operates without bias and ideally has minimal excess 1/f noise. This makes them more suited for high sensitivity applications compared to their resistive bolometer counterparts where 1/f noise can be a major limiting factor.

Detector design is an exercise in tradeoffs. Reducing the thermal conductance is a primary design objective for obtaining a good responsivity. Some important design choices that involve a tradeoff with thermal conductance are

- Number of thermocouple junctions N. Larger number of couples give a higher output voltage at the cost of increased thermal conductance.
- Electrical resistance of a support leg. Reducing the G by reducing the cross sectional area and increasing the length has the exact opposite effect on the device resistance and can lead to degradation in the Johnson noise.
- Thermal time constant $\tau = C/G$. A very low value of conductance can lead to a very high thermal time constant and low measurement bandwidth unless the heat capacity C is reduced proportionately. This reduction in C may be constrained by other factors like the detector absorption.

Hence detector design involves balancing many tradeoffs in the parameter space. A computer program can be used to calculate device performance for various geometries and different material parameters. It is also possible to perform some optimizations using MATLAB routines like *fminsearch()*.

A variety of thermoelectric materials have been used previously to demonstrate IR detection using radiation thermopiles [60, 61]. A good review of the underlying physics of the Seebeck effect and sensors based on this effect can be found in Graf [62] and van Herwaarden [63]. A list of the relevant physical properties of thermoelectric materials for design purposes are summarized in Table 4.1. The properties of semiconducting thin films are highly doping dependent and should

only be used as a guide. The parameters for Bi_2Te_3 and Sb_2Te_3 are typical for co-sputtered thin films deposited during this work.

Material	Thermal Conductivity (W/mK)	Resistivity ($\mu\Omega$-m)	Seebeck Coefficient (μV/K)
Bi [64]	8.1	1.1	72.8
Sb [64]	0.39	18.5	32
Al [65]	237	10	1.8
n-poly-Si [65]	28	0.03	110
n-polySi [66]	31.5	8.13	57
p-polySi [66]	31.2	2.21	103
Bi_2Te_3	0.3	7	45
Sb_2Te_3	0.3	17	105

Table 4.1: Physical properties of selected thermoelectric junction materials.

4.1.1 Example design

Several geometries were designed during the mask layout phase of this project. The central absorber structure was either 50, 100 or 150 μm in size. Each detector was constrained on all four corners since this arrangement has the highest mechanical stability. The detectors have either 1, 2 or 4 thermocouple junctions in series. The 1 and 2 couple detectors have lower voltage output but also have a lower thermal conductance. The 4 couple detectors have higher output voltage at the cost of a high conductance. The 1 and 2 couple designs have the thermocouples at the side of the absorber plate along with stabilizing support legs on the plate corners. The 4 couple designs have the thermocouples only at the corners. The 4 couple designs were found to be the most successful of all because of their higher output voltages.

In the detector mask layout the width of Sb_2Te_3 is set equal to or larger than width of the Bi_2Te_3 to account for the lower electrical conductivity of Sb_2Te_3. The width ratios of Bi_2Te_3 to Sb_2Te_3 are typically 1:1, 1:2 or 1:3. The detectors are grouped according to the etch hole size into quarters for uniform etch release. Two hole sizes, 756 μm and 1000 μm, used for low conductance designs cover most of the wafer area. A small section of 290 μm holes is also laid out for high conductance and high bandwidth designs. An image of a typical mask layout for a 4 pair series connected SbTe-BiTe couples in a 1000 μm etch hole is shown in Fig. 4.1. The

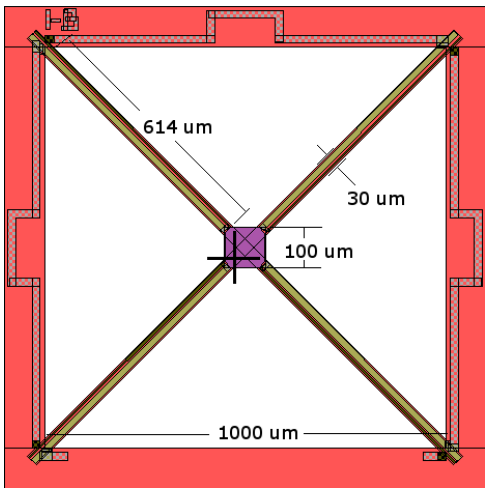

Figure 4.1: Mask file showing an example design. The parameters geometrical parameters and the design performance values are shown in Table 4.2.

central absorber structure consists of germanium and nickel and Al_2O_3 is assumed to be the mechanical support layer . The geometrical parameters and the design values for the detector performance are summarized in Table 4.2.

A note on test structures - Test structures for measurement of physical properties are integral to the mask layout. Design of test structures for measurement of semiconductor properties can be found in Schroeder [67]. Several test structures were included in the mask layout. These included structures for measurement of resistivity, contact resistance, Hall Effect structures for carrier concentration, Seebeck coefficient measurement of thermoelectric thin films and thermal conductance test structures.

4.1.2 Radiation Thermal conductance

The thermal conductance is the sum of the leg thermal conductance and the radiation thermal conductance. While the leg thermal conductance is straightforward to calculate, radiation thermal conductance calculations is a little more involved, especially for a spectrally dependent emissivity. For a grey body emitter with emissivity ϵ, the radiation thermal conductance is given by $G_{rad} = 8A_d\epsilon\sigma T^3$. For a spectrally selective absorber the correct expression needs to be computed from Planck's law.

Parameter	Value
Hole Width	1000 μm
Leg Length	614 μm
Leg Width	15 μm Sb_2Te_3, 5 μm Bi_2Te_3
Plate width	100 μm
Plate thickness	300 nm
Al_2O_3 thickness	50 nm
Thermoelectric thickness	400 nm
G (including radiation)	5.9×10^{-8} W/K
C	6.6×10^{-9} J/K
τ	0.112 msec
$\Re(\omega = 0)$	10,116 V/W
$D^*(\omega = 0)$	5.9×10^{9} cm$\sqrt{Hz}$ / W
NEP_J	1.9 pW
NEP_{TC}	0.45 pW
NEP_{BB} (Blackbody)	0.55 pW

Table 4.2: Physical properties of selected thermoelectric junction materials. Note - Photon noise NEP is assumed to be at the level of a 100 μm^2 blackbody for this design.

The power radiated by a spectrally selective body at temperature T of area A_d in a solid angle Ω over all wavelengths λ can be computed from Plank's law by

$$P_{rad} = \int_{\lambda,\Omega} \frac{2hc^2 A_d \epsilon(\lambda,\Omega) d\lambda d\Omega}{\lambda^5 [exp(hc/\lambda k_B T) - 1]} \tag{4.5}$$

where $\epsilon(\lambda,\Omega)$ is the spectrally and spatially dependent emissivity. The thermal conductance associated with this radiation heat transfer mechanism is given by the derivative of the radiated power with temperature

$$G_{rad}(T) = \frac{dP_{rad}}{dT} = \frac{2h^2c^3A_d}{k_B T^2} \int_{\lambda,\Omega} \frac{\epsilon(\lambda,\Omega) exp(hc/\lambda k_B T) d\lambda d\Omega}{\lambda^6 [exp(hc/\lambda k_B T) - 1]^2} \tag{4.6}$$

Equation 4.6 is the correct expression for radiation thermal conductance of a detector. For the purposes of designing the detector, a spectral and spatial emissivity of a multilayered structure can be obtained from the matrix multiplication method as explained in Chapter 3. This

emissivity can then be used in equation 4.6 for numerical integration to obtain the thermal conductance. Note that the radiation thermal conductance is a temperature dependent quantity.

4.2 Spectrally selective detector fabrication

A spectrally selective detector architecture has separate components for optical absorption and electrical transduction. The resonant absorber structure is a Fabry-Perot (FP) cavity, the design of which was discussed in detail in Chapter 3. Briefly, it consists of a highly reflecting back mirror and a lightly absorbing top mirror separated by an $m\lambda/2$ air gap. This is different from the more usual quarter wave anti-resonant optical cavity that boosts absorption across the entire 8-12 μm wavelength range [5]. The detector top mirror consists of a transparent germanium (Ge) center plate with an ultra-thin layer of nickel (Ni) that introduces a controllable absorption. The center plate is suspended from the substrate by low thermal conductance support legs which may contain BiTe/SbTe thermoelectric junctions. These thin films are encapsulated by a thin aluminum oxide (Al_2O_3) layer deposited by atomic layer deposition (ALD) which provides mechanical support for the structure.

Top Mirror and detector process flow

The fabrication of this detector is a two wafer process. The top mirror and thermoelectrics are fabricated on a thin double side polished silicon wafer. The fabrication process flow for the top detector wafer is indicated in Fig. 4.2(a-g) and is as follows

Base Layers - A thin ($\sim$250 μm) double side polished wafer is coated with a Low Pressure Chemical Vapor Deposition (LPCVD) low stress silicon nitride layer ($\sim$ 80nm) for electrical isolation. It is then coated with a thin ($\sim$ 22 nm) Al_2O_3 layer by Atomic Layer Deposition (ALD) at 250 °C.

Optical Absorber - Wafer is patterned with single layer LOR-3A resist spun on at 1500 rpm. Thin film of germanium (thickness $\sim$ 300 nm) and nickel ($\sim$ 3 nm) is deposited by DC magnetron sputtering at 250 °C temperature, 5 mTorr pressure and 20 sccm of Argon. These films are patterned using lift-off in hot 1165 resist stripper. The Ge-Ni stack is

encapsulated by 11 nm of ALD Al_2O_3 to protect it from the subsequent process steps.

Metallization layers - Wafer is metalized by evaporating a thin layer of titanium and platinum (5nm and 10nm) as thermoelectric contact metal and chromium and gold for bond pads for wire bonding. The metal layers are patterned using LOR-3A lithography and 1165 liftoff.

Thermoelectric layers - The BiTe and SbTe layers are deposited next using RF magnetron co-sputtering of constituent element targets of Bi, Te and Sb at elevated substrate temperatures and are patterned using LOR-3A liftoff process.

Encapsulation and front etch - Entire thin film stack is encapsulated in thin 20 nm ALD Al_2O_3 to protect it during subsequent etching. Front side Al_2O_3 is patterned using a BCl_3 plasma to define the detector geometry usign a Shipley 1813 photoresist mask. The etch recipe uses 30 sccm BCl_3, 615 Watts ICP power, 12 Watts RIE power, 2.3 mTorr chamber pressure. Instead of etching the entire film in a single step it is better if the etch is performed over several short cylces, each with a short etch step and a long idle step to prevent overheating and resist burn.

Backside patterning - A hard mask of Al_2O_3 ($\sim$ 100 nm) is deposited on the backside using e-beam evaporation. After ensuring that the front side is protected with photoresist, a front-to-back alignment is performed to pattern a photoresist mask on the backside. The backside is then etched using a combination of buffered oxide etch (BOE), BCl_3 dry etch and SF_6 silicon etch (STS etcher fastpoly recipe) to define a hard mask for subsequent etch release. BOE can cause severe undercut of resist and hence the wafer is etched in BOE short 2 minute steps, where after each step the wafer is rinsed and inspected for resist damage.

Etch release - Wafer is cleaved into quarters and one quarter is bonded to a dummy handle wafer using Cool Grease 7016. The grease is applied on all sides of the quarter in thin, uniform and bubble-free layer to ensure good cooling. The wafer is etched in Deep Reactive Ion Etching (DRIE) Bosch process. The etch is stopped before it etches all the way through the wafer. The last remaining etching are performed in a slow SF_6 RIE process (STS etch

slowpoly recipe), which etches most of the remaining silicon and the front side silicon nitride.

Die removal and clean - The etched quarter is carefully removed and flipped to get front side facing up. The thermal grease leaves significant residue on the front side. This residue is cleaned in oxygen plasma RIE (STS etch O2clean recipe).

Bottom mirror process flow and detector assembly

The bottom mirror is deposited on a custom SOI wafer. The process steps for back mirror fabrication and detector assembly are shown in Fig. 4.3(a)-(d).

SOI and base layers - The SOI wafer is fabricated using the fusion bonding a thick handle wafer to a thin silicon wafer using the process detailed in Chapter 3. The thin silicon wafer has a thickness similar to the top mirror / detector wafer. The bonded wafer is coated with ALD Al_2O_3 ($\sim$ 35 nm) at 250 C which functions as a hard mask.

Pillar etch - Al_2O_3 hard mask is patterned using BOE and the wafer is cut into quarters. Vertical pillars are etched in to the SOI wafer using DRIE Bosch process which stop on the buried oxide. Exposed buried oxide and Al_2O_3 hard mask are removed in BOE.

Mirror deposition - Pillar wafer is diced into squares using a wafer saw and attached to a handle wafer using Cool Grease CGR 7016. A hybrid metal - dielectric mirror stack is deposited on the pillars using thermal evaporation at 180 °C substrate temperature. Mirror stack consists of chromium ($\sim$ 60nm), sodium fluoride ($\sim$ 1.6 μm) and germanium ($\sim$ 480 nm).

Detector assembly - Top and bottom dies are aligned together in a flip chip bonder and are bonded with a room temperature curing epoxy (Thorlabs F120) which simultaneously functions as a spacer and an adhesive. After ensuring the spacings are correct the devices are wirebonded in a ceramic package using low power tack bonding. More details on this process can be found in section 3.2.5.

An SEM image of the assembled detector showing the principle components is shown in Fig. 4.3(e).

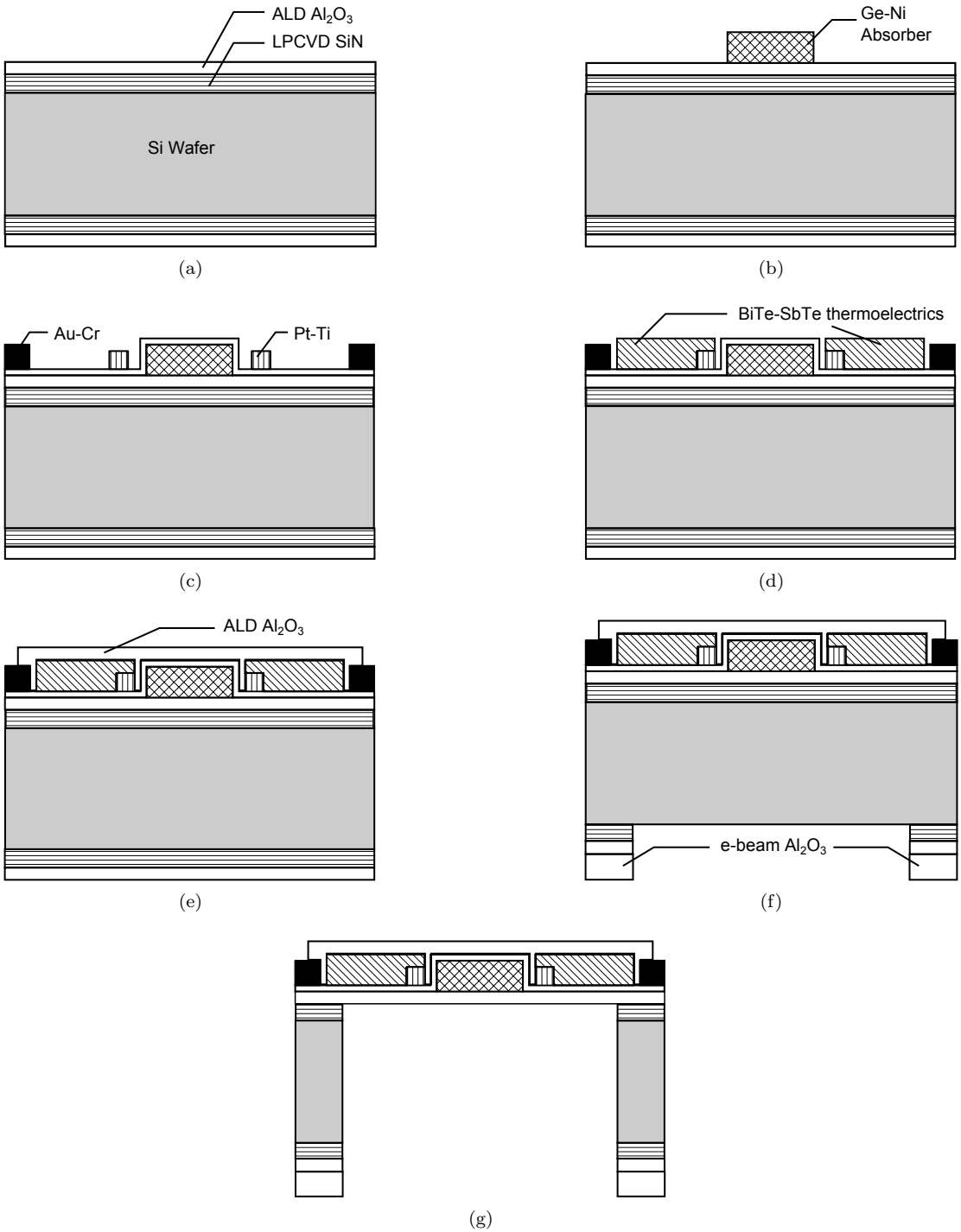

Figure 4.2: Top mirror and detector fabrication process flow

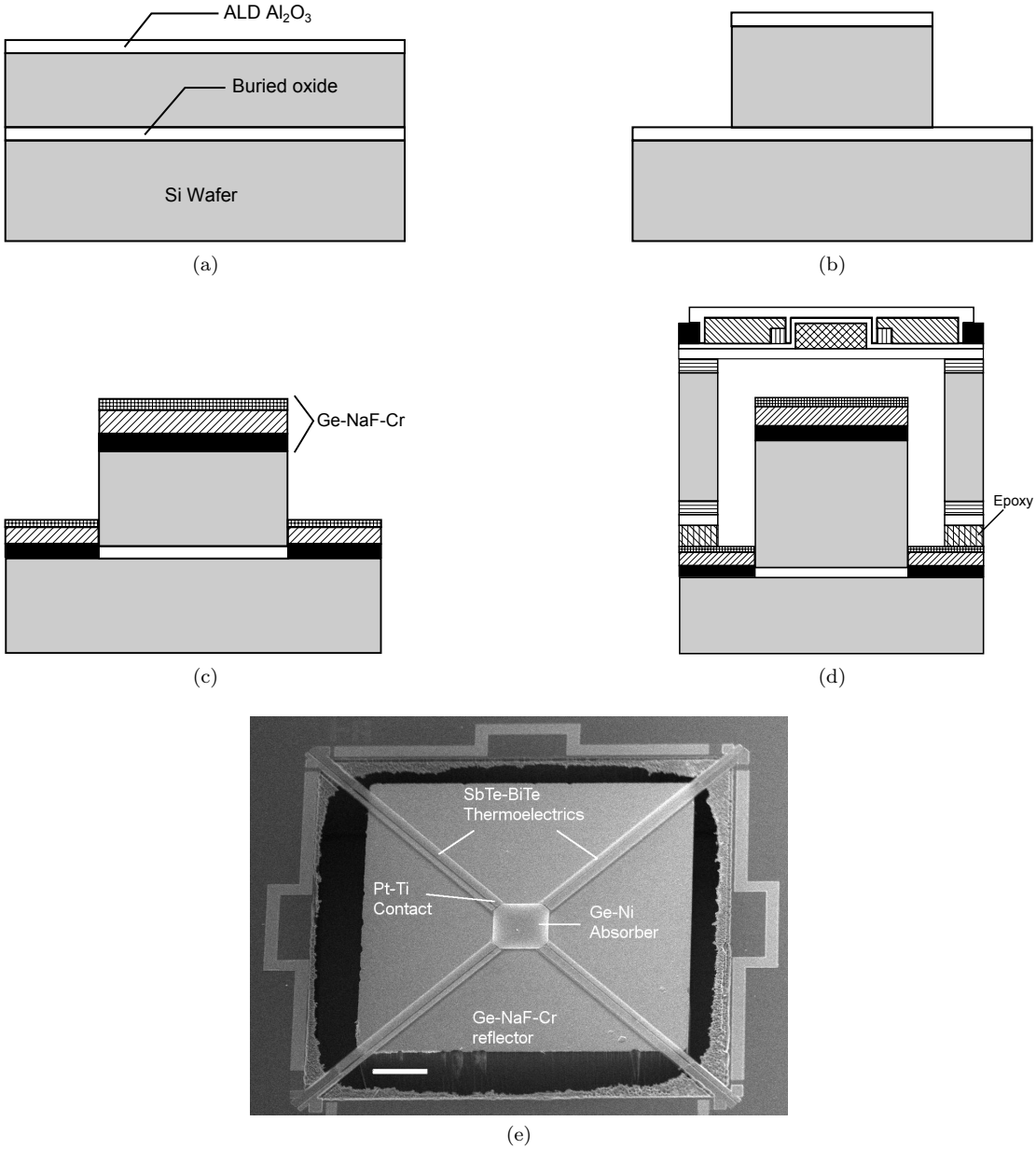

Figure 4.3: (a)-(d)Bottom mirror fabrication process flow and detector assembly. (e) SEM image of a fabricated detector.

Fabrication Challenges

Thermal damage - Etch release of the dies in DRIE is a challenging process. Inefficient thermal conduction from the etching wafer can lead to extensive heat damage to the thin films on the front side. The thermoelectric thin films and gold are most susceptible to damage. The damage is most apparent on the sides of the thermoelectric lines, on the overlap areas of the thermoelectric and platinum metalization and on the exposed gold areas.

Careful bonding of the quarter wafer to the dummy can mitigate the thermal damage. Cool grease CGR 7016 from Ai Technologies is used for this bonding. The grease is heated to 55 °C to soften and applied in a thin, uniform layer along the quarter perimeter. The bonded wafer is baked on a hotplate at 55 °C for 10 minutes and is left in the DRIE load lock vacuum for 5 minutes to remove all air bubbles. This is sufficient to ensure a good thermal contact.

Germanium damage - Germanium reacts with thermoelectric materials, possibly antimony telluride, and becomes highly susceptible to damage. This reacted germanium appears dark brown under a microscope, as opposed to the shiny gray of unreacted germanium. Once it reacts, the germanium film can get attacked by simple solvents like acetone. Encapsulation of germanium with ALD Al_2O_3 before exposure to any thermoelectric materials is necessary to prevent any damage.

Bottom mirror roughness - Large sized particulates can get attached to the surface of the bottom wafer during fusion bonding, as mentioned in chapter 3. These particulates act as scattering centers, thus reducing the cavity finesse. Since the fusion bonding chuck is the source of these particulates, a few dummy bonding runs should be done to remove as many particles as possible before an actual wafer bonding run.

4.3 Detector characterization

4.3.1 FTIR measurement

Several electrical and optical measurements have been done to estimate the performance of these devices. The resonant absorption of the cavity is verified in an FTIR reflectance microscope. A reflectance spectrum is measured from the center plate in the microscope after appropriate

spatial aperturing and compared to a background spectrum measured off an evaporated gold mirror. An absorption spectrum, A, is calculated from the reflectance spectrum, R, using $A = 1 - R$ assuming the transmission to be zero. Fig. 4.4 shows the normalized absorption spectrum measured from the center plate of two devices with different cavity lengths along with the response expected from a plane wave simulation. The absorption data is normalized such that the maxima and the minima lie between 0 and 1.

The device in Fig. 4.4a has a cavity length of 5.1 μm and has a fundamental resonance peak near 9000 nm and a second order peak near 5,500 nm wavelengths. The device in Fig. 4.4b has longer cavity length of 11.6 μm and thus has more orders appearing in the region of interest with the primary resonance occurring near 10,500 nm wavelength. Changing the air gap during device assembly gives us the flexibility to tune the resonance to a desired wavelength or to introduce additional resonances in a longer cavity. The peak positions match the simulated spectra, but the width of the resonance is much broader experimentally than theoretically. This larger-than-expected resonance width may be due to scattering losses in the back mirror and non-ideal absorption in the center plate.

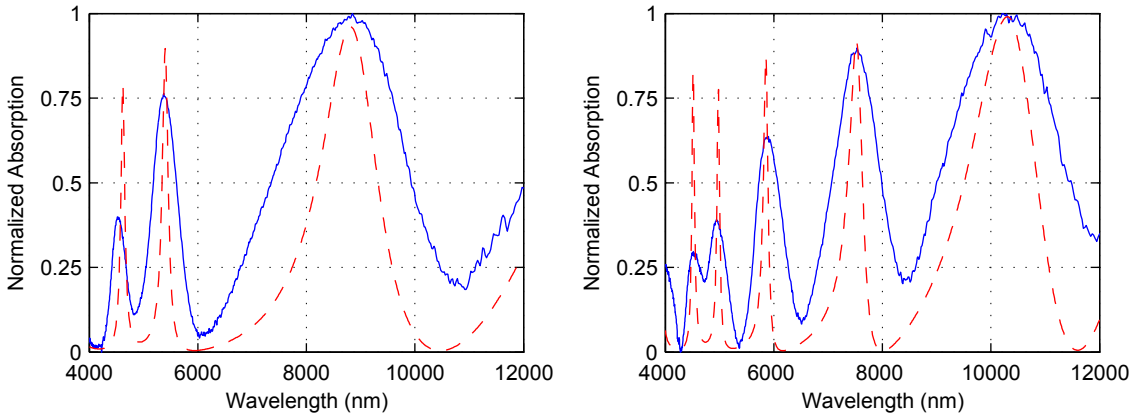

Figure 4.4: Absorption spectrum measurement (blue solid) and simulation (red dashes) from the center plate of a device in an FTIR microscope for two different cavity lengths.

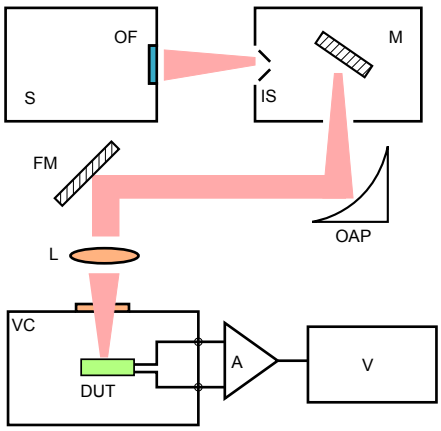

Figure 4.5: Schematic of the optical test setup. S - Source, OF - Order sorting filter, M - Monochromator, IS - Input shutter, OAP - Off axis parabolic mirror, FM - Folding mirror, L - Lens, VC - Vacuum chamber, DUT - detector, A - Amplifier, V - Voltmeter.

4.3.2 Responsivity measurement

The detector responsivity is measured as a function of the wavelength in a setup shown in Fig. 4.5. The detector is mounted in a vacuum chamber with an IR transmissive window. It is illuminated with an infrared thermal light source (Oriel Apex with IR element 6575). The output of the source is filtered through an order sorting filter (7.5 μm long pass) and a grating monochromator (Oriel Cornerstone 260, model 74100) with a 100 lines/mm grating blazed at 9 μm wavelength. The monochromator has an input shutter which can be used to modulate the input. The output of the monochromator is collimated with a gold coated 90 $^\circ$ off-axis parabolic mirror (effective focal length 7.62 cm), redirected with a gold coated folding mirror and finally focused through a ZnSe lens (focal length 5 cm). The electrical output voltage of the detector is fed into a custom built low noise amplifier (gain 1000x, see section 4.3.3) and the output of the amplifier is recorded by a DC voltmeter (Fluke 45).

The detector responsivity is measured near DC frequencies (f $\approx$ 0). At each wavelength the detector output is measured twice - first, with the detector under illumination and next, after closing a shutter at the monochromator input. For each shutter condition the response is averaged over 25 data points collected over the course of 5 seconds. This method enables us to determine the detector response to the source illumination alone and eliminate the effect of the

DC drifts that occur due to variation in the background conditions over time.

The incident radiation power is measured behind the vacuum window at the detector plane with a calibrated cooled HgCdTe (MCT) photoconductor (Electro-Optical Systems MCT10-0100). The output voltage of the MCT is multiplied by an interpolated wavelength dependent responsivity to obtain the wavelength dependent incident power. Assuming a uniform incident intensity, this incident power is multiplied by ratio of the two detector absorbing areas to obtain the incident illumination power over the area of the thermal detector center plate. The detector responsivity $\Re$ is then calculated by dividing the detector output voltage by the calculated incident input power. The specific detectivity D^* for a Johnson noise limited detector can then be calculated from equation 4.4.

The responsivity is first measured under flood illumination conditions with the entire detector receiving the incident radiation. The responsivity and detectivity of two devices of different geometries is shown in Fig. 4.6. The device in Fig. 4.6(a) has a resistance 15.1 kΩ with a nominal area of 100 μm $\times$ 100 μm of the center plate for calculations. A peak D^* of 4.4×10^9 cm $\sqrt{Hz}$/Watt is obtained for a responsivity of 6964 V/W. The device in Fig. 4.6 (b) has a resistance of 7.9 kΩ and a nominal area of 150 μm $\times$ 150 μm and has a peak detectivity of 4.7×10^9 cm $\sqrt{Hz}$/Watt and a responsivity of 3630 V/W. These two detectors have different cavity lengths which affects the width of the primary resonance.

The optical cavity coupling gives rise to two separate resonance effects in the measured response of the device shown in Fig. 4.6a. First, there is a primary absorption from the center plate which gives rise to the broad envelope of the spectral response. Second, there is some absorption in the thermoelectric legs which couples with the bottom of the pillar wafer to form a longer optical cavity. This gives rise to the rapid fluctuations which are superimposed on the primary resonance. The two regions that give these separate responses are shown in the microscope photograph of the detector in Fig. 4.7a. For the detector in Fig. 4.6(b) the back mirror is large enough to cover the entire detector including the center plate and the legs. The distance between the center plate and the mirror is the same as the distance between the legs and the mirror in this case. The observed response thus has a single resonance and has no rapid fluctuations from the legs. The absorption in the thermoelectric legs in this wavelength range is due to free carrier absorption in the highly doped semiconductors and is confirmed by FTIR

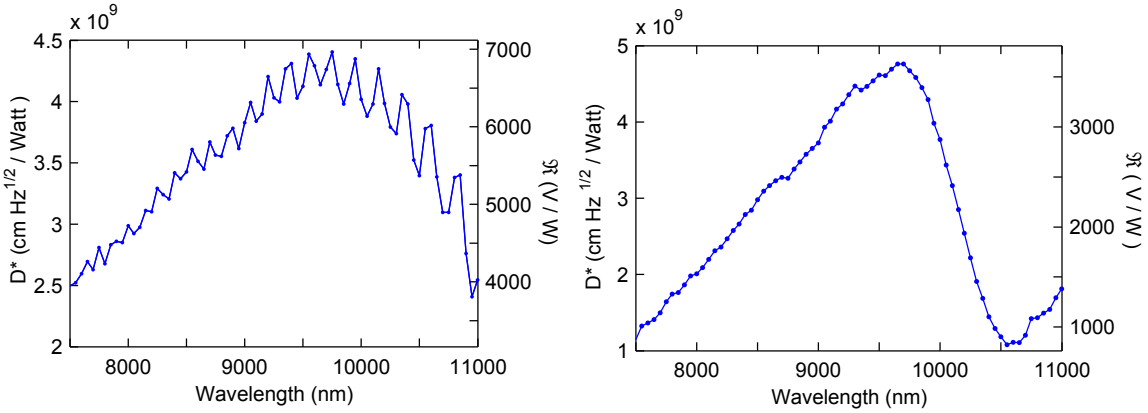

(a) (b)

Figure 4.6: Detectivity and responsivity of two devices under flood illumination (a) ∼100μm × 100 μm center plate, 15.1 kΩ resistance (b) ∼150 μm × 150 μm center plate, 7.9 kΩ resistance (color online).

reflectance and transmission spectra taken from the detector legs.

The absorption from the thermoelectric legs adds some uncertainty to the detectivity calculations since the detector effective area is now bigger than the actual geometric area of the center plate. To reduce this uncertainty the same detector is measured with an aperture. This aperture is made by etching holes through a silicon wafer and has an area of 200 μm×200 μm and is 250 μm thick. One side of the aperture is coated with aluminum to reduce any transmission through the silicon. This aperture is then aligned to the detector and fixed to the detector die at a very close distance to eliminate any diffraction effects. A confocal image of the detector and the aperture is shown in Fig. 4.7b. The imperfect alignment of the detector to the aperture and the high aspect ratio of the aperture reduces the incident radiation on the center plate, making the measured response a lower limit of the real response, just as the flood illumination data reported in Fig. 4.6 is an upper limit. The detectivities reported in Fig. 4.6 and 4.8 are some of the highest reported detectivities for spectrally selective thermal detectors.

The measured responsivity and detectivity for this detector after aperturing is shown in Fig. 4.8. We now measure a peak D* of 3×10^9 cm$\sqrt{Hz}$/Watt and a peak responsivity of 4700 V/W at 9350 nm. The resonant cavity enhances the absorption on resonance by as much as 2.5 times

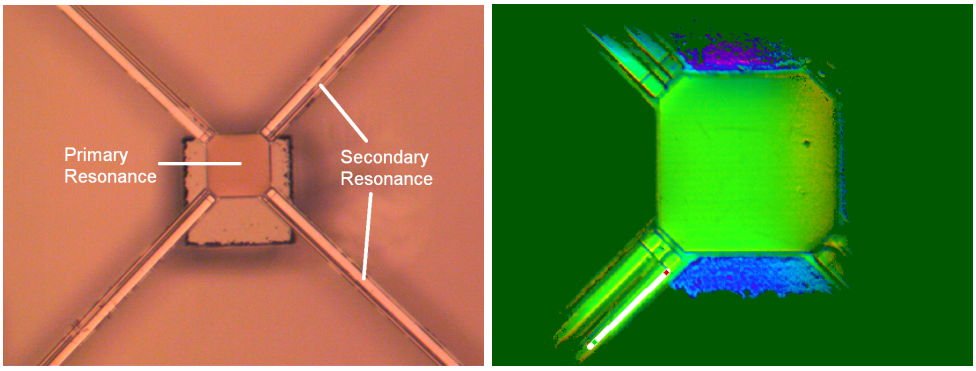

(a) (b)

Figure 4.7: (a) Photograph of the detector from Fig. 4.6a showing spatial regions corresponding to primary and secondary resonances. (b) Confocal image of a detector through a 200 μm $\times$ 200 μm aperture.

that off resonance. Also the secondary resonance peaks of Fig. 4.6(a) have been significantly reduced with the aperturing. This apertured detectivity can be seen as a lower limit for this detector with an effective area closer to the geometric area of the center plate.

4.3.3 Noise measurement techniques

Detector noise is a fundamental metric of its performance. The principle sources of noise in a thermal detector are electrical noise, thermal conductance noise and photon noise. The thermal conductance noise occurs due to temperature fluctuations in a body which is at equilibrium with a thermal sink while the photon noise occurs due to random fluctuations in the incoming stream of photons. The electrical noise consists of the fundamental Johnson noise of the resistor and any excess noise. With the exception of excess noise, all the other noise sources have a constant power spectral density across all frequencies i.e. their spectrum is "white". Excess noise has roughly a 1/f dependence on the frequency and is hence called 1/f noise.

The spectral density of electrical noise is given by

$$S_e(f) = S_{Johnson} + S_{1/f} = 4k_BTR + \frac{V_b^2\kappa}{f} \quad (V^2/Hz) \tag{4.7}$$

where k_B is the Boltzmann constant, T is the temperature, R is the device resistance, V_b

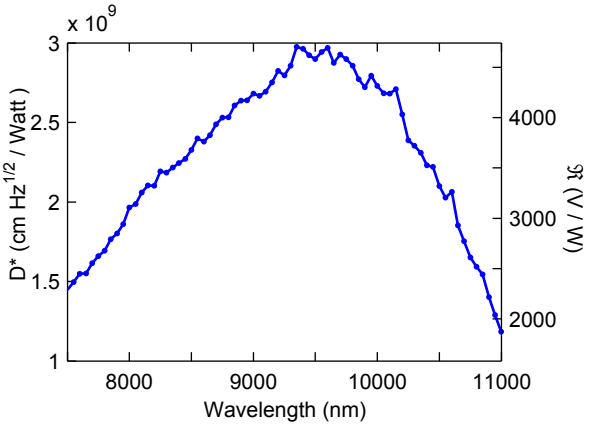

Figure 4.8: Detectivity and responsivity of device from Fig. 4.6a after aperturing.

is the bias voltage, κ is the Hooge parameter and f is the electrical frequency. The 1/f excess noise appears only when a bias current is flowing through the resistor and is a major limiting factor in resistive bolometers at low frequencies. The exact mechanism behind this 1/f noise not precisely known though several theories have been proposed [68, 69].

A thermoelectric readout scheme does not require a bias to operate and should not exhibit any 1/f noise when measured using a high input impedance amplifier. This is a major advantage of a thermoelectric readout over a resistive bolometer. A thermoelectric readout is ideally limited by the Johnson noise in its resistor. Johnson noise is a quantum effect and can be explained by deriving Planck's radiation law with a one dimensional density of states [70].

The measurement of low level device noise is a challenging task. The major difficulties are in amplifying weak signals to measurable levels and in proper shielding and grounding to eliminate environmental noise pickup. There are several sources in the literature that discuss measurement techniques and instrumentation details [71]. Several techniques for measurement of noise have been described in the literature including ac method using a lock-in amplifier [72], dc method using Fourier transform [73] and cross correlation methods [74].

The noise in thermoelectric IR detectors have been measured using a FFT dynamic signal analyzer (HP MODEL 35660) after appropriate amplification. The noise floor of this instrument is around 40 nV/$\sqrt{Hz}$ at low frequencies. Since this is higher than the Johnson noise level of a typical thermal detector, the use of amplifiers is necessary. Commercial amplifiers like

Stanford Research SR 560 has very high 1/f noise at low frequencies and is not suitable for this measurement. Custom amplifiers were constructed using off the shelf ICs for this purpose.

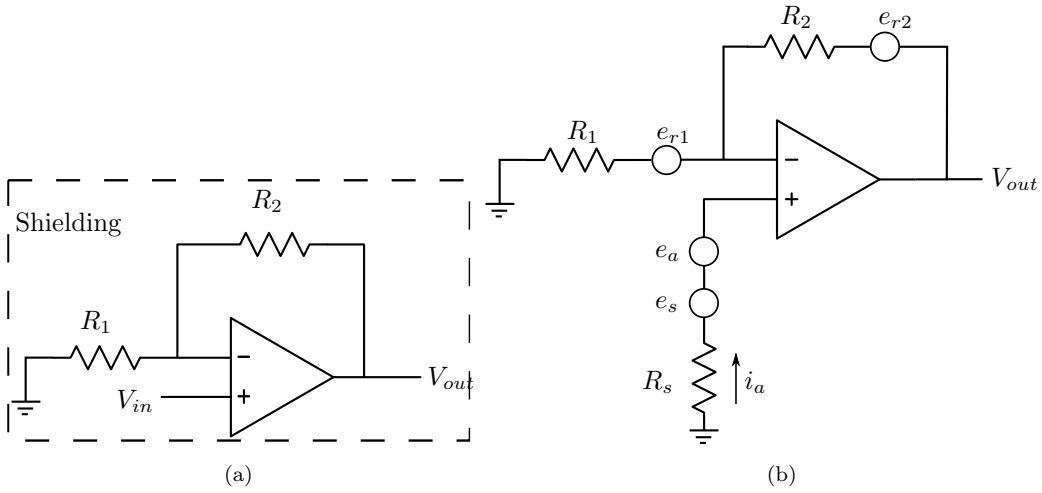

Figure 4.9: (a) Inverting amplifier for noise measurement (b) Schematic diagram of amplifier with all noise sources.

Fig. 4.9a shows the basic circuit diagram of a non-inverting amplifier with voltage gain $A_v = 1 + R_2/R_1$. The op-amp should not be configured in an inverting configuration because this degrades the input impedance. An equivalent circuit with all the component noise sources is shown in Fig. 4.9b. The noise sources are bias resistor noise e_{r1} and e_{r2}, the amplifier input voltage noise and input current noise e_a and i_a and the device noise e_s which is the quantity of interest. This detector noise is equal to $\sqrt{4k_BTR_s}$ for Johnson noise limited detector with source resistance R_s.

Since noise adds in quadrature, the total noise referred to the amplifier input is given

$$e_{tot}^2 = e_{r1}^2 + \frac{e_{r2}^2 R_1^2}{(R_1 + R_2)^2} + e_a^2 + (i_a R_s)^2 + e_s^2 \tag{4.8}$$

The noise from bias resistors can be minimized by good circuit design. The input resistance R_1 has the largest influence on the noise and should be of the lowest value possible. The desired amplifier gain then determines the value for R_2. Since the noise of R_2 appearing at the amplifier input is reduced by a voltage divider circuit its influence on the noise is minimal. Wirewound

resistors have the lowest noise and should be used for R_1 and R_2.

The amplifier input current noise and input voltage noise have the biggest influence on the total noise and should be minimized by careful selection of the amplifier. Two commercially available op-amps were selected for this purpose. The first amplifier is Analog Devices AD-743 JFET front end op-amp. This amplifier was selected because of its very low current noise and was found good for measurements above 2 Hz. However below this frequency this op-amp has unacceptable 1/f noise. For measurements at lower frequencies Analog Devices AD4528-1 op-amp was used. This amplifier uses a chopper stabilization technique to achieve negligible 1/f noise (see [75]).

The amplifier is constructed on a small perfboard that is mounted inside a small metal box for shielding. All signal inputs are grounded on the metal box to eliminate ground loops. The input to the shielded box uses standard coax cables that are twisted around each other to further reduce the 60 Hz pickup. The whole setup is battery powered to reduce power line noise coupling. The power spectral density is measured by the dynamic signal analyzer after the output is averaged over 10 measurements.

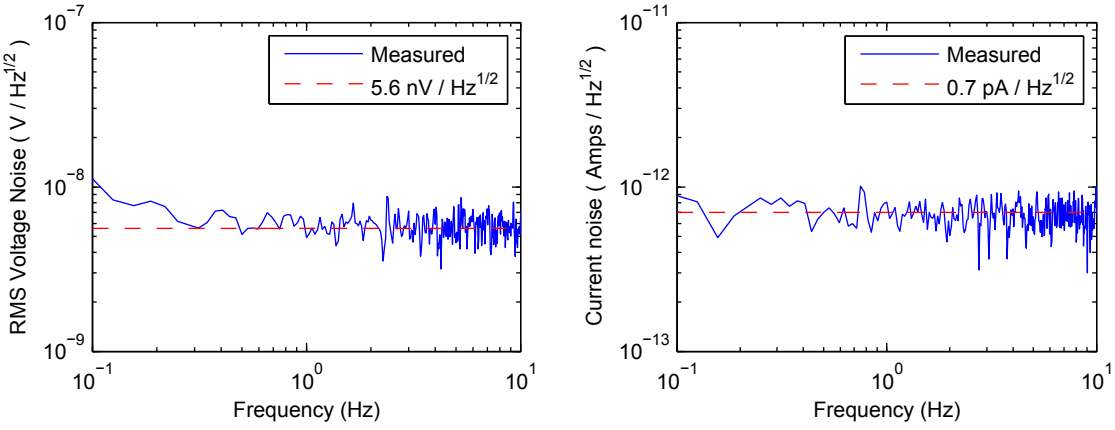

Figure 4.10: Measured noise for AD4528-1 op-amp (a) Voltage Noise (b) Current Noise. The dashed line shows values from manufacturer's datasheet.

The amplifier voltage and current noise are first measured. The voltage noise is measured by shorting the amplifier inputs together and measuring the output. If the noise from bias resistors

is neglected then the noise power in this case should just be the amplifier voltage noise and is shown in Fig. 4.10a. The current noise is measured by coupling a 200 kΩ precision metal film resistor to the input and measuring the output power spectral density. This resistor is free of excess noise and the output should be the quadrature sum of amplifier voltage noise, amplifier current noise and 200 $k\Omega$ resistor Johnson noise. From equation 4.8 the amplifier current noise can be calculated and is shown in Fig. 4.10b. A voltage noise of 5.6 nV/$\sqrt{Hz}$ and a current noise of 0.7 pA/$\sqrt{Hz}$ was measured which is exactly as expected from the manufacturer datasheet.

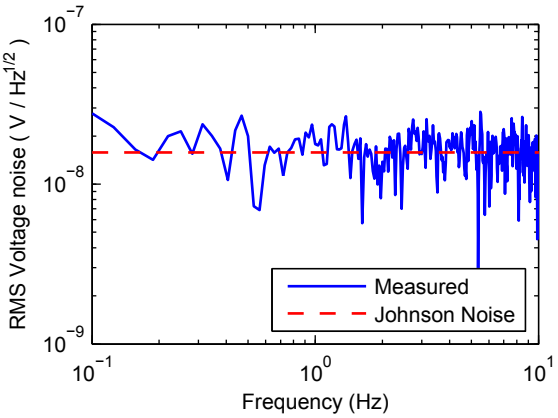

Figure 4.11: Measured noise from a thermal detector after subtracting amplifier noise. Dashed line shows the Johnson noise level for a 15.1 kΩ resistor.

The device output is measured after connecting the output from the vacuum chamber through coaxial cables to the amplifier inputs. The device is operated under vacuum for this measurement. The amplifier gain is set to 100x which gives a high enough amplification with a reasonable value of the DC offset. The amplifier voltage and current noise are subtracted from the total measured noise to obtain the device noise. This noise is found to be very close the Johnson noise predicted value for f ¿ 0.1 Hz as shown in Fig. 4.11. A strong DC signal from the detector makes it difficult to measure the noise frequencies lower than 0.1 Hz.

4.3.4 Thermal time constant measurement

The thermal time constants of these devices are also measured in an arrangement that is slightly modified from Fig. 4.5. Instead of a DC measurement, the output of the source is now modulated

using a mechanical chopper and the detector voltage is measured using a lock-in amplifier. The device output voltage is measured at several modulation frequencies of the chopper.

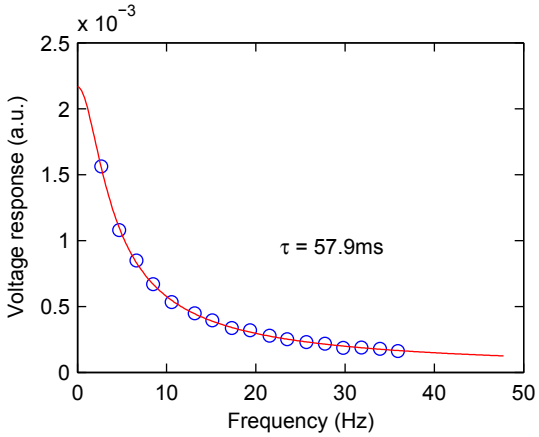

Figure 4.12: Time constant of the detector measured with chopper and lock-in amplifier showing the data (circles and Lorentzian fit (red solid line).

The output voltage of a thermal detector is given by equation 4.1 and shows a Lorentzian dependence to angular frequency ω. This measured output voltage from the lock-in amplifier is fit to Lorentzian curve using MATLAB *nlinfit()* routine. The thermal time constant is then extracted from this curve fit. The time constant of the device in Fig. 4.6(a) is found to be 58 msec as shown in Fig. 4.12.

4.3.5 Thermal conductance measurement using switched bias technique

Reducing the thermal conductance is of primary importance for achieving high detectivity thermal detectors and is an important detector performance metric. A thermal conductance measurement involves providing a known amount of heat to a body and measuring the corresponding temperature change. In resistive bolometers this measurement is straightforward and can be performed by heating the bolometer with Joule heating and measuring the corresponding change in bolometer resistance [76].

For thermoelectric detectors this measurement is not possible since there is no resistor on the detector plate for heating and temperature readout. An alternative method is to use the

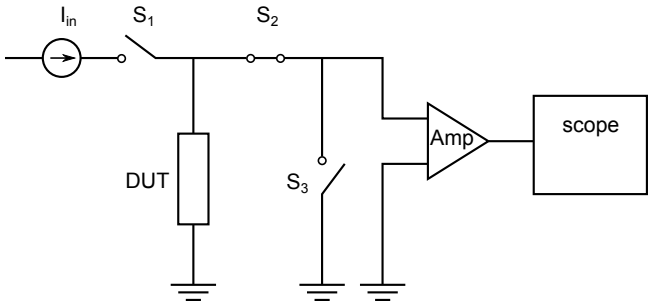

(a)

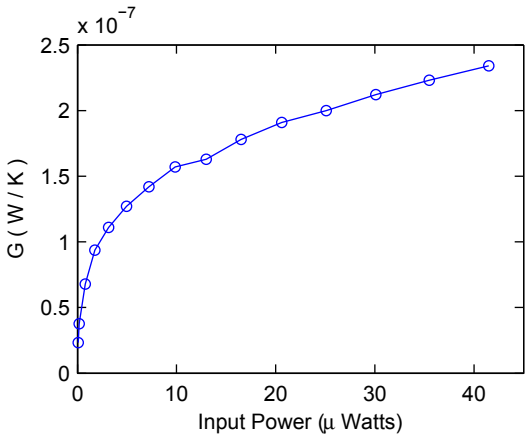

(b)

Figure 4.13: (a)Simplified circuit schematic for measuring thermal conductance. (b) Measured thermal conductance vs. input power assuming negligible Peltier heating.

Seebeck voltage developed at the thermoelectric junction due to the Joule heat dissipated at the junction itself. This is a slightly complicated measurement because the current source has to be disconnected from the circuit to measure the Seebeck voltage. This is the principle behind the switching technique for measuring detector thermal conductance [7]. The thermal detector is sourced with a current for one half cycle to produce Joule and Peltier heating in the device and is then disconnected. In the next half cycle the Seebeck voltage developed by the detector, which decays during the cycle, is measured immediately after the current source is disconnected. Assuming that half of the Joule heating is dissipated to center plate while the

other half is dissipated at the substrate, the thermal conductance can be written as

$$G = \frac{IV_{in}NS}{2V_T} + \frac{IV_{in}N^2S^2T_c}{V_T} \tag{4.9}$$

where I is the input current, V_{in} is the input voltage, N is the number of thermocouple junctions, S is the Seebeck voltage, T_c is the cold junction temperature and V_T is the measured thermoelectric voltage. The first term is a result of the Joule heating and the second term is due to the Peltier heating (or cooling if connected appropriately). It is usual to source a high current to the detector such that the Joule heating becomes dominant. In this case the effect of the second term can be ignored. Then if the Seebeck coefficient difference for the junction is known the thermal conductance can be calculated.

A simplified schematic of the circuit that implements this technique is shown in Fig. 4.13a. A constant current is supplied to the detector under vacuum using a Keithley 2410 source meter, which also measures the input voltage. The switches S_1, S_2 and S_3 are implemented using Analog Devices ADG453 CMOS switch IC. S_1, S_3 are modulated in phase with each other and out of phase with S_2 using a square wave generator at low frequencies (usually 1 Hz). The output is amplified using Stanford Research SR560 voltage preamplifier and recorded using a Tektronics oscilloscope.

The calculated thermal conductance with input power is shown in Fig. 4.13b. The conductance rises with input power due to increased radiation. The thermal conductance is estimated to be 2.3×10^{-7} W/K at an input power of 41 μ Watts, which is the last measurement point in Fig. 4.13b. This value is likely to be an overestimate because it is calculated for a high temperature difference condition between the detector and the substrate. This would enhance the radiation heat transfer from both the legs and the center plate significantly, leading to a higher value for the thermal conductance. The radiation thermal conductance of a 100μm square black body is 1.2×10^{-7} at 300 K which is close to the thermal conductance value measured for our detector.

Chapter 5

Effective area approximation for thermal detector characterization

The basic design of a thermal detector consists of an optical absorber and transducer connected to a substrate using low thermal conductance support structures. While designing such detectors, it is assumed, to first order, that all the optical absorption is localized to an absorber located on the main detector plate and that absorption is negligible in the supports. While this assumption is a reasonable approximation in many cases where the legs have strongly reflecting metallization, it breaks down for example, in a thermoelectric readout scheme, where doped semiconductor thermoelectric films on the support legs can have significant free carrier absorption in the long wave infrared [77, 78].

This absorption in the legs leads to some difficulty during detector characterization since it leads to uncertainty in the actual absorbing area. The responsivity of these detectors is usually measured under flood illumination from an incoherent thermal source where the incident beam spot size is poorly matched to the central absorber area. Optical techniques like spatial filtering to restrict the beam spot size can lead to an unacceptable loss of incident power. This problem of a poorly defined effective area is especially acute in detectors that are not in dense two-dimensional arrays. Here, the support legs may cover an area comparable to the central absorber or even larger. Rigorous optical modeling techniques utilizing full 2-D analytical solutions [79],

reduced dimension 1-D multi-zone thermal models [65, 80] and numerical methods including finite element modeling [81, 82] have been previously used to analyze and optimally design the detectors taking into account this leg absorption.

In this paper, we extend the modeling done previously [83, 84] to extract a simple effective area approximation for thermal detectors with absorption in the supports. The intent of the modeling is to obtain an accurate interpretation of the results of a responsivity measurement, rather than to optimize a detector in its design parameter space. This effective area can be directly substituted in place of the geometric area in standard equations to obtain the detector responsivity without the need for additional numerical modeling. This method can also be used to calculate the individual contribution of the legs and the center plate to the total generated response of the detector to incident radiation.

5.1 1-D model of leg absorption

This section develops a model for estimating an effective absorbing area of a thermal detector with absorbing support legs.

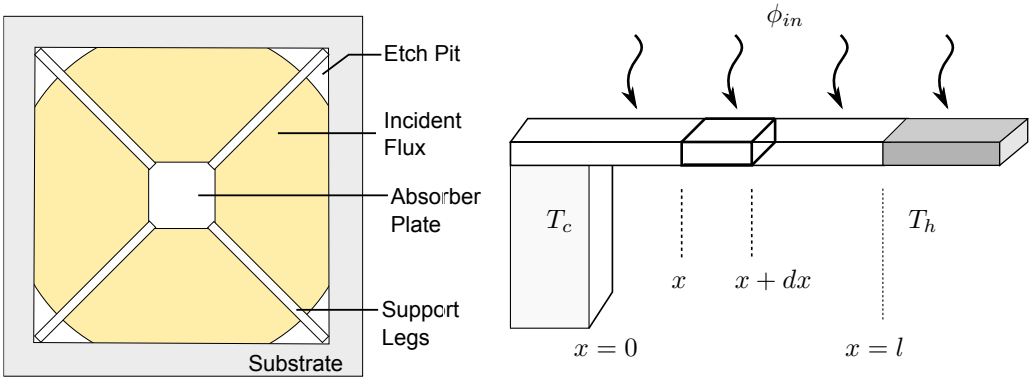

Figure 5.1: (a) Top view of the detector model with input flux illuminating the entire detector area (b) Cross sectional view of the detector model showing one leg.

A top view of a thermal detector is shown in Fig. 5.1a. It consists of a central absorbing plate of area A_p and emissivity ϵ_p which is suspended from the substrate with N absorbing legs

of width w_l, length l_l, thickness t_l, emissivity ϵ_l and thermal conductivity k_l. The symmetry of the structure can be exploited by analyzing the heat transfer through just one support leg. A cross section of one of the legs is shown in Fig. 5.1b. The thermoelectric leg extends from $x = 0$ to $x = l$. The center plate is assumed to be at uniform temperature T_h for $x > l$. The heat balance for a differential volume element dV with absorbing area dA at a distance x from the cold junction can be written as,

$$k_l \frac{d^2(T(x) - T_c)}{dx^2} - Q_o + Q_i = 0 \tag{5.1}$$

where T_c and T(x) are the temperatures of the cold junction and the temperature along the support leg, Q_o and Q_i are the volumetric heat output and input to the differential volume. The heat transfer mechanism is either through conduction or radiation, but not through convection for detectors operating under vacuum. If the incident radiation flux ϕ_{in} is assumed to be uniform across the entire device then

$$Q_i = \frac{\epsilon_l \phi_{in} dA}{k_l dV} \tag{5.2}$$

and Q_o is the volumetric heat lost to radiation given by

$$Q_o = \frac{2\epsilon_l \sigma (T(x) - T_c)^4 dA}{k_l dV} \tag{5.3}$$

where the factor of 2 accounts for radiation from both top and bottom surface. Substituting in equation 5.1 we have.

$$\frac{d^2(T(x) - T_c)}{dx^2} - \frac{2\epsilon_l \sigma (T(x)^4 - T_c^4)}{k_l t_l} + \frac{\epsilon_l \phi_{in}}{k_l t_l} = 0 \tag{5.4}$$

Assuming that the temperature change is small, this equation can be linearized around T_c to

$$\frac{d^2 \Delta T(x)}{dx^2} - \frac{8\epsilon_l \sigma T_c^3 \Delta T(x)}{k_l t_l} + \frac{\epsilon_l \phi_{in}}{k_l t_l} = 0 \tag{5.5}$$

where $\Delta T = T(x) - T_c$. This is a standard linear differential equation which as the following

solution.

$$\Delta T = Ae^{\sqrt{p}x} + Be^{-\sqrt{p}x} + \frac{q}{p} \tag{5.6a}$$

where

$$p = \frac{8\epsilon_l \sigma T_c^3}{k_l t_l} \tag{5.6b}$$

$$q = \frac{\epsilon_l \phi_{in}}{k_l t_l} \tag{5.6c}$$

The constants A and B can be determined using the boundary conditions

$$\Delta T(x) = 0 \quad \forall\ x = 0 \tag{5.7a}$$

$$\Delta T(x) = \Delta T_{net} = T_h - T_c \quad \forall\ x = l \tag{5.7b}$$

The term ΔT_{net} is the maximum temperature difference along the leg which is the temperature difference between the hot and the cold junctions. Substituting equation 5.6a into equations 5.7a and 5.7b, the constants A and B obtained after some algebraic manipulation are

$$A = \frac{\Delta T_{net} - q/p(1 - e^{-\sqrt{p}l})}{2\sinh(\sqrt{p}l)} \tag{5.8a}$$

$$B = \frac{-\Delta T_{net} + q/p(1 - e^{\sqrt{p}l})}{2\sinh(\sqrt{p}l)} \tag{5.8b}$$

$$\tag{5.8c}$$

Substituting these into equation 5.6a and rearranging the terms, the temperature distribution along a support leg can then be written as

$$\Delta T(x) = \left[\Delta T_{net} - \frac{q}{p}\right] \frac{\sinh(\sqrt{p}\ x)}{\sinh(\sqrt{p}\ l)} + \frac{q}{p}\left[1 + \frac{\sinh(\sqrt{p}\ (x-l))}{\sinh(\sqrt{p}\ l)}\right] \tag{5.9}$$

The coefficient p is the ratio of the radiative losses to the conduction losses in the leg and has dimensions of 1/area. The coefficient q is a measure of the heat absorbed in the leg normalized

to conduction losses and has the dimensions of Kelvins / m^2. Equation 5.9 gives the temperature distribution across a leg for a non-zero leg emissivity under a uniform illumination flux.

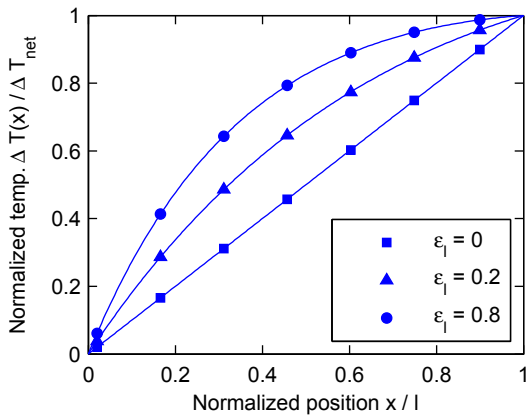

Figure 5.2: Normalized temperature difference along the length of a support leg for different ϵ_l and with $\epsilon_p = 0.25$.

The normalized temperature difference along a support leg as given by equation 5.9 is plotted in Fig. 5.2 for a plate emissivity of 0.25. For non-absorbing legs ($\epsilon_l = 0$), the temperature varies linearly along the leg. When the legs start absorbing, the temperature difference rises faster. The figure indicates increasing contribution of the legs to the signal since large sections of the legs are now at a temperature closer to that of the plate.

The net voltage signal generated in the thermopile detector will be a function of the maximum temperature difference between the hot and cold junctions, ΔT_{net}. This quantity can be calculated from the heat balance at $x = l$ by

$$Nk_l w_l t_l \frac{d\Delta T}{dx}\bigg|_{x=l} = A_p \epsilon_p \phi_{in} - 8A_p \epsilon_p \sigma T_c^3 \Delta T_{net} \tag{5.10}$$

Equation 5.10 simply balances the heat absorbed and radiated from the center plate to the heat flowing out through the support legs at $x = l$. Note that in this simplified model the effects of conduction in the center plate are neglected and the entire region for $x > l$ is assumed to be at a constant temperature. The heat balance given by equation 5.10 would not be valid if there are significant conduction effects in the center plate, in which case the maximum temperature will no longer be at the end of the support leg.

The net temperature difference between the hot and the cold junctions can be written as

$$\Delta T_{net} = \frac{A_p \epsilon_p \phi_{in} + \frac{q}{\sqrt{p}} N k_l w_l t_l \left\{ \frac{\cosh(\sqrt{p}\ l) - 1}{\sinh(\sqrt{p}\ l)} \right\}}{8 A_p \epsilon_p \sigma T_c^3 + N k_l w_l t_l \sqrt{p} \coth(\sqrt{p}\ l)} \tag{5.11}$$

Examining this equation 5.11 it can be seen that the net temperature difference of is a sum of two individual temperature components, one of which is from the center plate and the other from the support legs. After substituting the values of p and q from equations 5.6b and 5.6c into equation 5.11, these individual plate and leg component contributions can be written as

$$\Delta T_{net} = \Delta T_{net}^{plate} + \Delta T_{net}^{leg} \tag{5.12a}$$

where

$$\Delta T_{net}^{plate} = \frac{A_p \epsilon_p \phi_{in}}{G_{eff}} \tag{5.12b}$$

$$\Delta T_{net}^{leg} = \frac{N w_l \phi_{in}}{G_{eff}} \sqrt{\frac{\epsilon_l k_l t_l}{8 \sigma T_c^3}} \left\{ \frac{\cosh(\sqrt{p}\ l) - 1}{\sinh(\sqrt{p}\ l)} \right\} \tag{5.12c}$$

and

$$G_{eff} = 8 A_p \epsilon_p \sigma T_c^3 + N k_l w_l t_l \sqrt{p} \coth(\sqrt{p}\ l) \tag{5.12d}$$

The denominator of equation 5.11 is written as G_{eff} since it is functionally equivalent to an effective thermal conductance which takes into account the conduction losses from the legs and radiation losses from the plate and the legs.

Some general features are immediately apparent from equation 5.11. The temperature difference ΔT_{net} depends more strongly on the plate emissivity ϵ_p than leg emissivity ϵ_l. It depends on the area of the plate but only on the width of the legs. If the leg consists of a sandwich of several films, the leg thermal conductivity k_l is an effective thermal conductivity given by

$$k_l = \frac{1}{w_l t_l} \sum_i k_i w_i t_i \tag{5.13}$$

The voltage signal generated by the detector depends on the net temperature difference between the hot and the cold junctions given by equation 5.11. This equation can be used to formulate a net "effective" absorbing area, A_{eff} of the detector which is different from the center plate area. Recognizing that the net temperature difference generated in a thermal detector is just the ratio of absorbed power P_{abs} to its thermal conductance G, equation 5.11 can be written as

$$\Delta T_{net} = \frac{P_{abs}}{G} = \frac{\phi_{in}\epsilon_p A_{eff}}{G_{eff}} \tag{5.14}$$

Comparing equation 5.14 to equation 5.11 and substituting the value of q from equation 5.6c, the effective area of the detector can finally be written as

$$A_{eff} = A_p + \frac{N\epsilon_l w_l}{\epsilon_p\sqrt{p}}\left[\frac{\cosh(\sqrt{p}l) - 1}{\sinh(\sqrt{p}l)}\right] \tag{5.15}$$

It can be seen from equation 5.15 that for a non-zero emissivity, this effective area is always

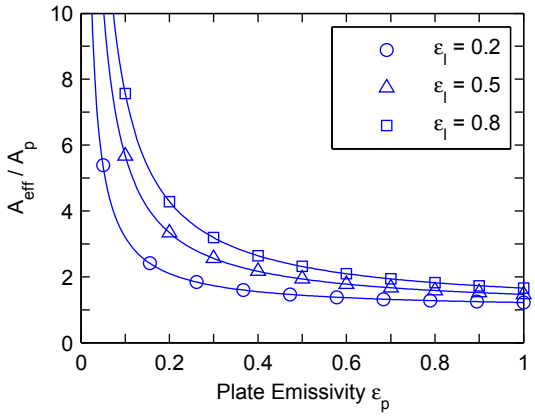

Figure 5.3: Ratio of effective area of a detector to the geometric plate area vs. absorber emissivity for various leg emissivities.

larger than the geometric area of the center plate. This effective area is a function of the device geometry as well as material properties of constituent components. In Fig. 5.3 the ratio of the effective area to the plate geometric area A_{eff}/A_p is plotted versus the plate emissivity for leg emissivities of 0.2, 0.5 and 0.8. The geometry used for this simulation is typical for our thermoelectric detector design. The center absorber plate is 150 μm$\times$ 150 μm and is suspended

by 4 legs which are 470 μm$\times$ 30 μm$\times$ 0.54 μm with a thermal conductivity of 0.47 W/mK. It can be seen that the ratio of the effective area to the plate area is always greater than 1 even for a modest leg emissivity and a high plate emissivity. For low plate emissivities the effective area can be significantly higher than the geometric area of the absorber. The minimum effective area for a particular ϵ_l can be found by substituting $\epsilon_p = 1$ in equation 5.15. It can also be seen that the detector fill factor is actually larger than expected from purely geometrical considerations and can be expressed in terms of the effective area.

This effective area can now be used to calculate the responsivity and the detectivity of the detector when the entire detector area receives illumination. The voltage output from the detector can be written as

$$V_{out} = NS\Delta T = \frac{NS\epsilon_p\phi_{in}A_{eff}}{G_{eff}} \tag{5.16}$$

where S is the difference in the Seebeck coefficients of the thermoelectric junction materials. The responsivity is the ratio of the voltage output to the incident power P_{in}.

$$\Re = \frac{V_{out}}{P_{in}} = \frac{V_{out}}{\phi_{in}A_{eff}} = \frac{NS\epsilon_p}{G_{eff}} \tag{5.17}$$

Thus the responsivity can be calculated by measuring the detector output voltage and the incident radiant flux and substituting the calculated effective area in equation 5.17. If the Seebeck coefficient of the thermoelectric legs is also known then this responsivity can be used to calculate a value for the effective thermal conductivity. This effective thermal conductance includes the effect of radiative heat transfer and is difficult to compute directly from other methods. The detectivity is the Noise Equivalent Power (NEP) normalized to the effective area and the detector bandwidth. For a detector with mean squared noise voltage of $\langle \Delta V^2 \rangle$ within an electrical bandwidth of Δf the detectivity is now given by

$$D^* = \Re\sqrt{\frac{A_{eff}\Delta f}{\langle \Delta V^2 \rangle}} = \frac{\Delta V_{out}}{\phi_{in}}\sqrt{\frac{\Delta f}{A_{eff}\langle \Delta V^2 \rangle}} \tag{5.18}$$

Thus the effective area from equation 5.15 can be used in a straightforward manner to calculate the responsivity and the detectivity if the emissivity of the plate and the support legs are known. Also since the effective area is always greater than the geometric center plate area, the use of

effective area in equations 5.17 and 5.18 will lead to a lower value for the detector responsivity and detectivity compared to the use of the detector plate area alone.

5.2 Experimental verification

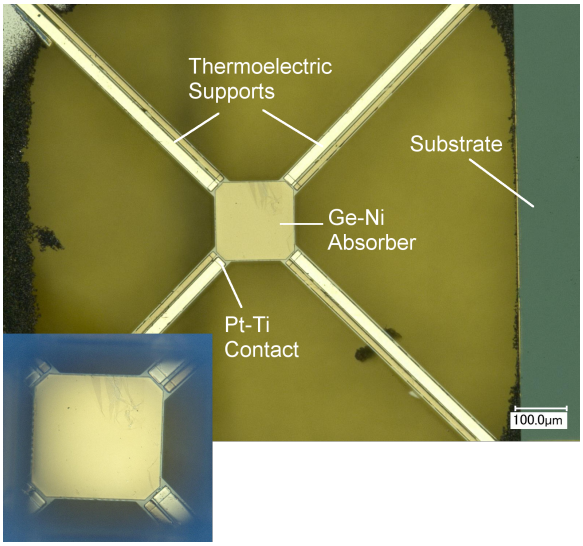

Figure 5.4: Microscope image of a finished detector showing its principle elements. Scale bar on the bottom right equals 100 μm. Inset shows an image of center plate as seen through a 200 μm $\times$ 200 μm aperture.

To test the model we have fabricated a set of thermal detectors as shown in the optical microscope image of Fig. 5.4. These fabrication and characterization of these detectors was discussed in detail in Chapter 4. These thermal detectors were designed for optical coupling with a resonant cavity to achieve spectrally selective absorption. This particular geometrical design was chosen to ensure optical flatness over fill factor. This design decision leads to a large area of the thermoelectric support legs compared to the center plate.

The emissivities of the various thin film regions of the detector are measured in the infrared using an FTIR microscope. The microscope is used to measure reflectance R and transmittance T from small spatial regions of the detector using an aperture. The absorptivity A can be calculated from the FTIR measurement since A = 1-R-T. This absorptivity is equal to the

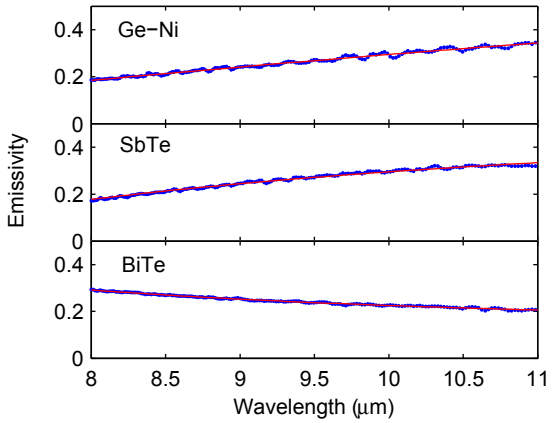

Figure 5.5: Emissivities calculated from FTIR reflectance and transmittance measurements for germanium-nickel, antimony telluride and bismuth telluride. The solid line is a second-order polynomial fit to the data.

emissivity from Kirchoff's law. The measured emissivity is shown for germanium-nickel, antimony telluride, and bismuth telluride in Fig. 5.5 and lies between 0.15 and 0.35 in the region of interest. The solid line shows second-order polynomial fits to the measured emissivity data. The effective emissivity of the antimony telluride and bismuth telluride composite leg is calculated as an average of the measured emissivities weighted by the respective areas.

The thermal conductivity of the ALD Al_2O_3 and the thermoelectric thin films is measured using specialized test structures. The thermal conductivity is found to be 1.75 W/mK for Al_2O_3 and 0.32 W/mK for the thermoelectric films. The thermal conductivity of these films are lower than those measured in the literature [85] which could be an due to the differences in film thickness and deposition conditions. The measured values along with the device geometry are then used to calculate an effective area using equation 5.15.

The wavelength dependent effective area was found to lie approximately between 2.3 and 1.9 times the center plate area as show in Fig. 5.6a. The individual contribution of the center plate and the legs to the total temperature signal can also be calculated from equation 5.12 and is shown in Fig. 5.6b. At lower wavelengths the legs contribute about 10% more to the signal than the center plate, while at higher wavelengths the situation is reversed and the plate contribution is around 5% higher at 11 μm. The variation in the individual contributions with wavelength is due to the variation in the emissivities with wavelength.

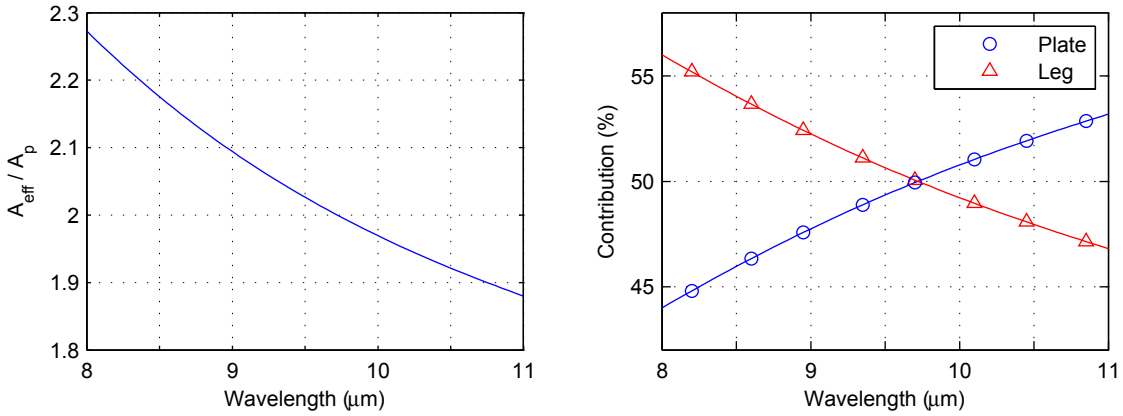

Figure 5.6: (a) Ratio of the effective area to geometrical center plate area calculated using equation 5.15 for device shown in Fig. 5.4. (b) shows the percentage Contribution of the leg (triangles) and the plate (circles) to the total signal.

To verify the accuracy of the effective area approximation, the responsivity of the detector shown in Fig. 5.4 is measured in an infrared optical test bench, similar to that used in Chapter 4 for time constant measurement. The detector is wire bonded and mounted in a vacuum chamber with an AR coated IR transmissive window. A ceramic thermal light source is filtered with a grating monochromator with 50 nm spectral width. The output of the monochromator is collimated using a parabolic mirror and focused on the detector using a zinc selenide lens. The incident flux is measured using a calibrated cooled HgCdTe photoconductor. The illumination spot size is large and overfills the entire area for both detectors. Spatial filtering of the monochromator output can be used in principle to reduce the spot size such that it underfills the detector areas but leads to unacceptable degradation of the monochromator output power.

The voltage output of the detector is measured using a chopper and lock-in amplifier arrangement. A custom built voltage preamplifier is used to condition the detector output. The measured output voltage and the input flux is then used to calculate the responsivity with different values for detector area in equation 5.17. These areas are (a) the center plate area (b) total detector area including thermoelectrics (c) effective area calculated from 5.15. The different areas of the detector components are measured using a digital optical microscope. The result of

the responsivity measurement is plotted in Fig. 5.7a and 5.7b.

The responsivity is first calculated using either the center plate area (21 687 μm^2) or the total area including the thermoelectric legs (84 613 μm^2). These areas are measured accurately using a Keyence digital optical microscope. This instrument allows selection of arbitrary spatial regions in an optical image and measure their areas. When the small center plate area is used, the calculated responsivity is high and is an overestimate. This is plotted as triangles in Fig. 5.7a. The small fluctuations in the measured responsivity are likely due to the formation of a weak optical cavity with the gold-coated bottom of the ceramic package. If the entire detector area including the thermoelectric legs is used in calculations the calculated responsivity is much lower due to the large area and is clearly is an underestimate. This is plotted as circles in Fig. 5.7a.

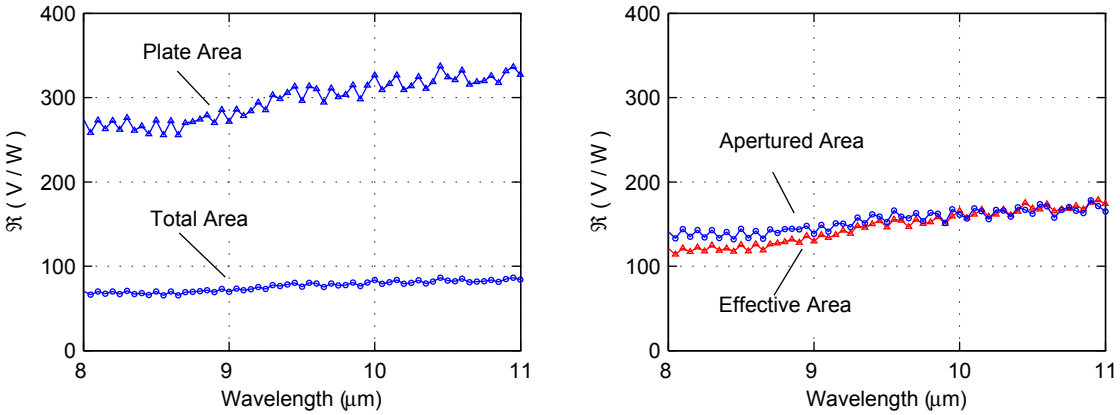

Figure 5.7: Responsivities calculated from measured detector output voltage using area equal to (a) center plate area (△) and total area (○) including thermoelectrics (b) effective area from equation 5.15 (△) and apertured detector (○) with area physically restricted to that of the center plate.

The responsivity is then calculated using the effective area and is plotted as triangles in Fig. 5.7b. To verify the accuracy of the effective area formalism, the detector absorbing area is physically restricted using a lithographically defined aperture stop. This aperture is 200μm $\times$ 200μm in size and is fabricated using DRIE etching of thin silicon wafers. One side of the aperture is metallized with aluminum to eliminate transmission through the silicon. This

aperture is then aligned with the detector die using a flip chip bonder system and attached directly to the detector die. An image of the detector through this aperture is shown in the inset of Fig. 5.4. It can be seen that the area of the detector is now essentially restricted to the center plate area. The voltage output of the detector is now measured again after aperturing, and the responsivity is calculated using the center plate area which is shown as circles line in Fig. 5.7b.

This apertured responsivity is the most accurate experimental estimate of the actual responsivity of the center plate since the absorbing area is tightly constrained. It can be seen that the responsivity calculated from the apertured detector matches closely with the responsivity calculated using an effective area. The two results are approximately within 15 % at lower wavelengths while the match is almost perfect at higher wavelengths. The responsivities calculated with just the plate area and with the total area 5.7a have a much larger error, differing by as much as a factor of two. Thus, the effective area approximation gives the most accurate estimate of the device responsivity.

We have thus derived a simple effective area approximation and verified its validity for the determination of thermal detector responsivity. The emissivity of various thin film regions is the biggest source of error in this computation. The FTIR measurement of reflectance and transmission does not account for scattering which could be significant at lower wavelengths due to film surface roughness. The other parameters like device geometry can be measured with good accuracy. This approximation can be used to quickly estimate a detector performance under flood illumination without requiring the use of complicated optical techniques.

Chapter 6

Conclusions and Future Work

This thesis presented several aspects of spectral selectivity pertinent to uncooled detectors operating in the long wave infrared. The issues that were discussed were both fundamental and applied in nature. In chapter 2 it was shown with theoretical arguments and numerical simulations that the ultimate limit of sensitivity of thermal detectors due to photon noise is increased when the detector absorption is limited spatially and spectrally. A theoretical construction using resonant cavity absorption was used to demonstrate these advantages. The detection limits of such a theoretical detector was explored in context of passive standoff detection of gaseous molecules.

In chapter 3 several practical aspects of design and fabrication of resonant cavity absorbers was discussed. Using two cavity configurations it was shown that spectrally selective absorption can be achieved with multi-layered thin films structures. Since these multi-layered designs use ultra-thin metallic films to introduce controllable absorption, a technique for measurement of refractive index of thin metallic films in the infrared was described. A two wafer fabrication and die bonding process was used to fabricate a resonant optical cavity and spectrally narrow absorption was demonstrated.

Chapter 4 discussed the design, fabrication and characterization issues related to high detectivity thermal detectors with thermoelectric readout. A specific design example was used to illustrate general principles of designing thermopile detectors for the infrared. Subsequently,

this design was integrated with a resonant cavity absorber using a MEMS fabrication process. Several challenging process integration issues were solved during the course of device fabrication. These devices were measured in custom infrared test bench and shown to have a spectrally dependent detectivity of at least 3×10^9 cm$\sqrt{\text{Hz}}$ / Watt. The instrumentation for performing various measurements like responsivity, noise and thermal conductance was described.

Finally chapter 5 discussed a simple method for measuring the responsivity of thermal detectors with absorption in the legs, which is a property of detectors with thermoelectric readout. Using this method, a simple approximation was derived which could be used to estimate responsivity by direct substitution in standard equations. This method was experimentally verified to give results within 15 % of the accurate responsivity.

6.1 Future work

The detectors presented in this thesis have a detectivity that is an order of magnitude lower than the blackbody photon noise limit. In order to reach, and even exceed this limit, improvements will be required on several fronts. First, it is necessary to reduce the full width half maximum of the absorption resonance of current detectors by improving finesse of the optical cavity. There are some challenges in achieving this with the current cavity design. It is difficult to obtain a desired properties and process repeatability with ultra-thin metallic films. Also the absorber layer thicknesses cannot exceed a certain limit due to time constant considerations. Alternate absorption methods like surface plasmon resonance structures and more complex cavity designs like a three mirror cavity are possible routes for achieving narrower resonance widths.

Second, further improvements in detector responsivity without any degradation in electrical noise would be necessary to achieve higher detectivities. Responsivity gains can be obtained by a combination of reduction in thermal conductance and improvements in the Seebeck coefficients of the thermoelectric materials. Thermal conductance reduction can be realized by using longer and narrower legs with thinner thermoelectric materials. Thermoelectric films with higher Seebeck coefficients have been demonstrated in the literature, though for much thicker films. Hence these improvements would be challenging from a process development perspective, but considerable gains can be realized with time and effort.

Finally, from an application point-of-view it would be desirable if these detectors could be integrated into linear and two dimensional arrays. The ability to dynamically tune the mirror spacings to scan across a range of wavelengths would be an added advantage. The fabrication process outlined in this thesis would not be suitable for this purpose because in a two wafer bonding process it is difficult to obtain micrometer level bonding uniformity. A monolithic surface micromachining process with tightly controlled thin film layer thicknesses would be more suitable for array development.

References

[1] Aleksandar D. Rakic, Aleksandra B. Djurisic, Jovan M. Elazar, and Marian L. Majewski. Optical properties of metallic films for vertical-cavity optoelectronic devices. *Applied Optics*, 37(22):5271–5283, 1998.

[2] Edward D. Palik. *Handbook of Optical Constants of Solids*. Academic Press, 1st edition, October 1997.

[3] B. E. Cole, R. E. Higashi, and R. A. Wood. Monolithic two-dimensional arrays of micromachined microstructures for infrared applications. *Proceedings of the IEEE*, 86(8):1679–1686, 1998.

[4] G.K. Fedder, R.T. Howe, Tsu-Jae King Liu, and E.P. Quevy. Technologies for cofabricating MEMS and electronics. *Proceedings of the IEEE*, 96(2):306–322, 2008.

[5] Sebastien Becker, Pierre Imperinetti, Jean-Jacques Yon, Jean-Louis Ouvrier-Buffet, Valrie Goudon, Antoine Hamelin, Claire Vialle, and Agns Arnaud. Latest pixel size reduction of uncooled IR-FPA at CEA, LETI. *Proc. SPIE 8541, Electro-Optical and Infrared Systems: Technology and Applications IX*, pages 85410C–85410C, October 2012.

[6] S. Sedky, P. Fiorini, M. Caymax, C. Baert, L. Hermans, and R. Mertens. Characterization of bolometers based on polycrystalline silicon germanium alloys. *IEEE Electron Device Letters*, 19(10):376 –378, October 1998.

[7] M.C. Foote, E.W. Jones, and T. Caillat. Uncooled thermopile infrared detector linear arrays with detectivity greater than 10^9 cmHz$^{1/2}$/W. *IEEE Transactions on Electron Devices*, 45(9):1896 –1902, September 1998.

[8] Yong-Hee Han, Kun-Tae Kim, Hyun-Joon Shin, Sung Moon, and In-Hoon Choi. Enhanced characteristics of an uncooled microbolometer using vanadiumtungsten oxide as a thermometric material. *Applied Physics Letters*, 86(25):254101–254101–3, June 2005.

[9] D.S. Tezcan, S. Eminoglu, and T. Akin. A low-cost uncooled infrared microbolometer detector in standard CMOS technology. *IEEE Transactions on Electron Devices*, 50(2):494 – 502, February 2003.

[10] A. Rogalski, J. Antoszewski, and L. Faraone. Third-generation infrared photodetector arrays. *Journal of Applied Physics*, 105(9):091101–091101–44, May 2009.

[11] Shinpei Ogawa, Kazuya Okada, Naoki Fukushima, and Masafumi Kimata. Wavelength selective uncooled infrared sensor by plasmonics. *Applied Physics Letters*, 100(2):021111–021111–4, January 2012.

[12] Thomas Maier and Hubert Brueckl. Multispectral microbolometers for the midinfrared. *Optics Letters*, 35(22):3766–3768, November 2010.

[13] Martin Arnold, Dmitry Zimin, and Hans Zogg. Resonant-cavity-enhanced photodetectors for the mid-infrared. *Applied Physics Letters*, 87(14):141103–141103–3, September 2005.

[14] A. J. Keating, K. K. M. B. D. Silva, J. M. Dell, C. A. Musca, and L. Faraone. Optical characterization of fabry-perot MEMS filters integrated on tunable short-wave IR detectors. *IEEE Photonics Technology Letters*, 18(9):1079 –1081, 2006.

[15] Yuyan Wang, Benjamin J. Potter, and Joseph J. Talghader. Coupled absorption filters for thermal detectors. *Optics Letters*, 31(13):1945–1947, July 2006.

[16] Warren A. Holmes, James J. Bock, Brendan P. Crill, Timothy C. Koch, William C. Jones, Andrew E. Lange, and Christopher G. Paine. Initial test results on bolometers for the planck high frequency instrument. *Applied Optics*, 47(32):5996–6008, November 2008.

[17] Peter R. Griffiths and James A. de Haseth. Signal-to-noise ratio. In *Fourier Transform Infrared Spectrometry*, page 161175. John Wiley & Sons, Inc., 2006.

[18] P B Fellgett. *The theory of infra-red sensitivities and its application to investigations of stellar radiation in the near infra-red*. Ph.D., University of Cambridge, Peterhouse (United Kingdom), England, 1952. U245287.

[19] Lee W. Schumann and Terrence S. Lomheim. Infrared hyperspectral imaging fourier transform and dispersive spectrometers: comparison of signal-to-noise-based performance. *Proc. SPIE 4480*, Imaging Spectrometry VII:1–14, January 2002.

[20] Michael R. Descour. Throughput advantage in imaging fourier-transform spectrometers. *Proc. SPIE 2819*, Imaging Spectrometry II:285–290, November 1996.

[21] R. Glenn Sellar and Glenn D. Boreman. Comparison of relative signal-to-noise ratios of different classes of imaging spectrometer. *Applied Optics*, 44(9):1614–1624, March 2005.

[22] Tomas Hirschfeld. Quantitative FT-IR: a detailed look at the problems involved. In *Fourier Transform Infrared Spectrometry: Applications to Chemical Systems*, volume 2. Academic Press, 1979.

[23] R. Clark Jones. The ultimate sensitivity of radiation detectors. *Journal of the Optical Society of America*, 37(11):879–888, November 1947.

[24] P. B. Fellgett. On the ultimate sensitivity and practical performance of radiation detectors. *Journal of the Optical Society of America*, 39(11):970–976, November 1949.

[25] W. B. Lewis. Fluctuations in streams of thermal radiation. *Proceedings of the Physical Society*, 59(1):34, January 1947.

[26] K. M. van Vliet. Noise limitations in solid state photodetectors. *Applied Optics*, 6(7):1145–1169, July 1967.

[27] E.H. Putley. Radiation shielding for uncooled detectors. *Infrared Physics*, 21(3):173–179, May 1981.

[28] P. L Richards. Bolometers for infrared and millimeter waves. *Applied Physics Reviews*, 1994(1):7–7, January 1994.

[29] J. M. Lamarre. Photon noise in photometric instruments at far-infrared and submillimeter wavelengths. *Applied Optics*, 25(6):870–876, March 1986.

[30] Jean-Mac Theriault, Eldon Puckrin, Francois Bouffard, and Bernhard Dery. Passive remote monitoring of chemical vapors by differential fourier-transform infrared radiometry: results at range of 1.5 km. *Applied Optics*, 43(6):1425–1434, 2004.

[31] William J. Marinelli, Christopher M. Gittins, Alan H. Gelb, and B. David Green. Tunable fabry-perot etalon-based long-wavelength infrared imaging spectroradiometer. *Applied Optics*, 38(12):2594–2604, April 1999.

[32] S. Chandrasekhar. *Radiative Transfer*. Dover Publications, 1960.

[33] Robert Siegel. *Thermal Radiation Heat Transfer*. Taylor & Francis, 4 edition, December 2001.

[34] R. M. Goody and Y. L. Yung. *Atmospheric Radiation: Theoretical Basis*. Oxford University Press, USA, 2 edition, December 1995.

[35] Dennis F. Flanigan. Detection of organic vapors with active and passive sensors: a comparison. *Applied Optics*, 25(23):4253–4260, December 1986.

[36] Dennis F. Flanigan. Vapor-detection sensitivity as a function of spectral resolution for a single lorentzian band. *Applied Optics*, 34:2636–2639, 1995.

[37] Avishai Ben-David, Janon F. Embury, and Charles E. Davidson. Radiative transfer model for aerosols in infrared wavelengths for passive remote sensing applications. *Applied Optics*, 45(26):6860–6875, 2006.

[38] L.S. Rothman, I.E. Gordon, A. Barbe, D.Chris Benner, P.F. Bernath, M. Birk, V. Boudon, L.R. Brown, A. Campargue, J.-P. Champion, K. Chance, L.H. Coudert, V. Dana, V.M. Devi, S. Fally, J.-M. Flaud, R.R. Gamache, A. Goldman, D. Jacquemart, I. Kleiner, N. Lacome, W.J. Lafferty, J.-Y. Mandin, S.T. Massie, S.N. Mikhailenko, C.E. Miller,

N. Moazzen-Ahmadi, O.V. Naumenko, A.V. Nikitin, J. Orphal, V.I. Perevalov, A. Perrin, A. Predoi-Cross, C.P. Rinsland, M. Rotger, M. imekov, M.A.H. Smith, K. Sung, S.A. Tashkun, J. Tennyson, R.A. Toth, A.C. Vandaele, and J. Vander Auwera. The HITRAN 2008 molecular spectroscopic database. *Journal of Quantitative Spectroscopy and Radiative Transfer*, 110(910):533–572, June 2009.

[39] Philip W. Morrison. Calculation of gas spectra for quantitative fourier transform infrared spectroscopy of chemical vapor deposition. *Journal of The Electrochemical Society*, 145(9):3212, 1998.

[40] David W. T. Griffith. Synthetic calibration and quantitative analysis of gas-phase FT-IR spectra. *Appl. Spectrosc.*, 50(1):5970, January 1996.

[41] Alexander Berk, Gail P. Anderson, Prabhat K. Acharya, Lawrence S. Bernstein, Leon Muratov, Jamine Lee, Marsha Fox, Steve M. Adler-Golden, James H. Chetwynd, Jr., Michael L. Hoke, Ronald B. Lockwood, James A. Gardner, Thomas W. Cooley, Christoph C. Borel, Paul E. Lewis, and Eric P. Shettle. MODTRAN5: 2006 update. *Proc. SPIE 6233, Algorithms and Technologies for Multispectral, Hyperspectral, and Ultraspectral Imagery XII*, pages 62331F–62331F–8, 2006.

[42] Herman van de Stadt and Johan M. Muller. Multimirror fabry-perot interferometers. *Journal of the Optical Society of America A*, 2(8):1363–1370, August 1985.

[43] Pochi Yeh. *Optical Waves in Layered Media*, volume 95 of *Wiley Series in Pure and Applied Optics*. Wiley, 1988.

[44] H. K. Pulker. Characterization of optical thin films. *Applied Optics*, 18(12):1969–1977, June 1979.

[45] Jennifer D. Traylor Kruschwitz and Walter T. Pawlewicz. Optical and durability properties of infrared transmitting thin films. *Applied Optics*, 36(10):2157–2159, April 1997.

[46] L. N. Hadley and D. M. Dennison. Reflection and transmission interference filters. *Journal of the Optical Society of America*, 37(6):451–453, June 1947.

[47] C. Hilsum. Infrared absorption of thin metal films. *Journal of the Optical Society of America*, 44(3):188, March 1954.

[48] P. B. Johnson and R. W. Christy. Optical constants of transition metals: Ti, V, Cr, Mn, Fe, Co, Ni, and Pd. *Physical Review B*, 9(12):5056–5070, June 1974.

[49] E. L. Green and L. Muldawer. Optical properties of the alpha-phase alloys Ag-Zn and Ag-Cd. *Physical Review B*, 2(2):330–340, July 1970.

[50] Neville V. Smith. Optical constants of sodium and potassium from 0.5 to 4.0 eV by split-beam ellipsometry. *Physical Review*, 183(3):634–644, July 1969.

[51] J.R. Nestell and R. W. Christy. Derivation of optical constants of metals from thin-film measurements at oblique incidence. *Applied Optics*, 11(3):643–651, March 1972.

[52] Michel Cathelinaud, Frederic Lemarquis, and Claude Amra. Index determination of opaque and semitransparent metallic films: Application to light absorbers. *Applied Optics*, 41(13):2546–2554, May 2002.

[53] Goran S Matijasevic, Chin C Lee, and Chen Y Wang. Au-Sn alloy phase diagram and properties related to its use as a bonding medium. *Thin Solid Films*, 223(2):276–287, February 1993.

[54] Pauline Renoux, Sigurdur Aegir Jonsson, Levente J. Klein, Hendrik F. Hamann, and Snorri Ingvarsson. Sub-wavelength bolometers: Uncooled platinum wires as infrared sensors. *Optics Express*, 19(9):8721–8727, April 2011.

[55] Jong-Wook Kim, Jae-Eung Oh, Seong-Chul Hong, Chung-Hoon Park, and Tae-Kyung Yoo. Room temperature far infrared ($8 \sim 10$ μm) photodetectors using self-assembled InAs quantum dots with high detectivity. *IEEE Electron Device Letters*, 21(7):329 –331, July 2000.

[56] Joseph J. Talghader, Anand S. Gawarikar, and Ryan P. Shea. Spectral selectivity in infrared thermal detection. *Light: Science & Applications*, 1(8):e24, 2012.

[57] David D. Skatrud and Paul W. Kruse, editors. *Uncooled Infrared Imaging Arrays and Systems, Volume 47*. Academic Press, October 1997.

[58] P. W. Kruse, L. D. McGlauchlin, and R. B. McQuistan. *Elements of Infrared Technology*. John Wiley {&} Sons, 1962.

[59] John C. Mather. Bolometer noise: nonequilibrium theory. *Applied Optics*, 21(6):1125–1129, March 1982.

[60] F. Vlklein, A. Wiegand, and V. Baier. High-sensitivity radiation thermopiles made of Bi-Sb-Te films. *Sensors and Actuators A: Physical*, 29(2):87–91, November 1991.

[61] A. Schaufelbuhl, N. Schneeberger, U. Munch, M. Waelti, O. Paul, O. Brand, H. Baltes, C. Menolfi, Qiuting Huang, E. Doering, and M. Loepfe. Uncooled low-cost thermal imager based on micromachined CMOS integrated sensor array. *Journal of Microelectromechanical Systems*, 10(4):503–510, 2001.

[62] A Graf, M Arndt, M Sauer, and G Gerlach. Review of micromachined thermopiles for infrared detection. *Measurement Science and Technology*, 18(7):R59R75, July 2007.

[63] A.W. Van Herwaarden and P.M. Sarro. Thermal sensors based on the Seebeck effect. *Sensors and Actuators*, 10(34):321–346, November 1986.

[64] J. Schieferdecker, R. Quad, E. Holzenkmpfer, and M. Schulze. Infrared thermopile sensors with high sensitivity and very low temperature coefficient. *Sensors and Actuators A: Physical*, 47(13):422–427, March 1995.

[65] Dehui Xu, Bin Xiong, and Yuelin Wang. Modeling of front-etched micromachined thermopile IR detector by CMOS technology. *Journal of Microelectromechanical Systems*, 19(6):1331 –1340, December 2010.

[66] M. Strasser, R. Aigner, C. Lauterbach, T.F. Sturm, M. Franosch, and G. Wachutka. Micromachined CMOS thermoelectric generators as on-chip power supply. *Sensors and Actuators A: Physical*, 114(23):362–370, September 2004.

[67] Dieter K. Schroder. *Semiconductor Material and Device Characterization*. John Wiley & Sons, February 2006.

[68] Richard F. Voss and John Clarke. Flicker (1/f) noise: Equilibrium temperature and resistance fluctuations. *Physical Review B*, 13(2):556–573, January 1976.

[69] F.N. Hooge and A.M.H. Hoppenbrouwers. 1/f noise in continuous thin gold films. *Physica*, 45(3):386–392, December 1969.

[70] Charles Kittel and Herbert Kroemer. *Thermal physics*. Macmillan, 1980.

[71] Henry W. Ott. *Noise Reduction Techniques in Electronic Systems, 2nd Edition*. Wiley-Interscience, 2 edition, March 1988.

[72] John H. Scofield. ac method for measuring low-frequency resistance fluctuation spectra. *Review of Scientific Instruments*, 58(6):985–993, June 1987.

[73] C. Leemann, M.J. Skove, and E.P. Stillwell. Excess "1/f" noise in bismuth whiskers. *Solid State Communications*, 35(2):97–100, July 1980.

[74] S. Demolder, M. Vandendriessche, and A. Van Calster. The measuring of 1/f noise of thick and thin film resistors. *Journal of Physics E: Scientific Instruments*, 13(12):1323, December 1980.

[75] Analog Devices. AN-1114 application note.

[76] P. Eriksson, J.Y. Andersson, and G. Stemme. Thermal characterization of surface-micromachined silicon nitride membranes for thermal infrared detectors. *Journal of Microelectromechanical Systems*, 6(1):55–61, 1997.

[77] I. G. Austin. Infra-red faraday rotation and free carrier absorption in Bi_2Te_3. *Proceedings of the Physical Society*, 76(2):169, August 1960.

[78] R. Sehr and L.R. Testardi. The optical properties of p-type Bi_2Te_3-Sb_2Te_3 alloys between 2-15 microns. *Journal of Physics and Chemistry of Solids*, 23(9):1219–1224, September 1962.

[79] Alexander G. Kozlov. Analytical modelling of steady-state temperature distribution in thermal microsensors using fourier method: Part 1. theory. *Sensors and Actuators A: Physical*, 101(3):283–298, October 2002.

[80] C. Escriba, E. Campo, D. Estve, and J.Y. Fourniols. Complete analytical modeling and analysis of micromachined thermoelectric uncooled IR sensors. *Sensors and Actuators A: Physical*, 120(1):267–276, April 2005.

[81] C. G. Mattsson, K. Bertilsson, G. Thungstrm, H.-E. Nilsson, and H. Martin. Thermal simulation and design optimization of a thermopile infrared detector with an SU-8 membrane. *Journal of Micromechanics and Microengineering*, 19(5):055016, May 2009.

[82] Chung-Nan Chen and Wen-Chie Huang. A CMOS-MEMS thermopile with low thermal conductance and a near-perfect emissivity in the 8 - 14-μm wavelength range. *IEEE Electron Device Letters*, 32(1):96–98, January 2011.

[83] F Volklein, G Min, and D.M. Rowe. Modelling of a microelectromechanical thermoelectric cooler. *Sensors and Actuators A*, 75(2):95, 1999.

[84] T. Elbel, R. Lenggenhager, and H. Baltes. Model of thermoelectric radiation sensors made by CMOS and micromachining. *Sensors and Actuators A: Physical*, 35(2):101–106, December 1992.

[85] Nicholas T. Gabriel and J.J. Talghader. Thermal conductivity and refractive index of hafnia-alumina nanolaminates. *Journal of Applied Physics*, 110(4):043526–043526–8, August 2011.

Appendix A

Appendix

This chapter contains some of the MATLAB code listing that was developed during the course of this thesis.

A.1 Multilayered Code

This code is an efficient, vectorized method for evaluating reflectance and transmssion through a multilayered thin film stack. For a detailed discussion of the method, see Yeh [43]. The code given below only show the calculations for s-polarization for brevity.

```
%%%%%%%%%%%%%%%% START OF MAIN PROGRAM %%%%%%%%%%%%%%%%%%%%%%%%%%
[nr, nc] = size(layermat);
j = sqrt(-1);           %Use j instead of i
%Define a row vector of complex indices
cindex(:,1) = layermat(:,1)-(j*layermat(:,3));
%%%% First Initialize the matrix %%%%%%
Ms_new_11 = 1; Ms_new_12 = 0; Ms_new_21 = 0; Ms_new_22 = 1;
Mp_new_11 = 1; Mp_new_12 = 0; Mp_new_21 = 0; Mp_new_22 = 1;

% Now loop through all layers but analyze all wavelengths at once
```

```
for i=2:nr-1
%Calculate angles here making sure that everything is complex
%compute angles using Snell's Law
  ctheta = asin(cindex(1).*sin(theta)/cindex(i));
  % Now initialize the M matrix for the next layers using previous layer
    Ms_11 = Ms_new_11;
    Ms_12 = Ms_new_12;
    Ms_21 = Ms_new_21;
    Ms_22 = Ms_new_22;
  % D matrix for s-wave
    Ds_11 = 1;
    Ds_12 = 1;
    Ds_21 = cindex(i).*cos(ctheta);
    Ds_22 = -cindex(i).*cos(ctheta);
  % Phase in the layer
    phi = 2*pi*cindex(i).*cos(ctheta).*layermat(i,2)./lambda;   %k*d
  % Propagation Matrix P
    P_11 = exp(j.*phi);
    P_12 = 0;
    P_21 = 0;
    P_22 = exp(-j.*phi);
  % Now multiply everything out for s polarization
    Prod_11 = (Ds_11.*(P_11.*Ds_22 - P_12.*Ds_21) +...
Ds_12.*(P_21.*Ds_22 - P_22.*Ds_21))...
./(Ds_11.*Ds_22 - Ds_12.*Ds_21);
% Similar multiplications can be carried out for other matrix elements
% Prod_12, Prod_21, Prod_22
  % Now multiply these products with the existing M matrix
    Ms_new_11 = Ms_11.*Prod_11 + Ms_12.*Prod_21;
    Ms_new_12 = Ms_11.*Prod_12 + Ms_12.*Prod_22;
```

```
    Ms_new_21 = Ms_21.*Prod_11 + Ms_22.*Prod_21;
    Ms_new_22 = Ms_21.*Prod_12 + Ms_22.*Prod_22;
end         %end of for
ctheta = asin(cindex(1)*sin(theta)/cindex(nr));
%If Total Internal Reflection in the last layer
%then change the sign of n*cos(theta)
if(imag(cindex(nr)*cos(ctheta))<=0)
    Ds_11 = 1; Ds_12 = 1;
    Ds_21 = cindex(nr).*cos(ctheta);
    Ds_22 = -cindex(nr).*cos(ctheta);
    Dp_11 = cos(ctheta); Dp_12 = cos(ctheta);
    Dp_21 = cindex(nr); Dp_22 = -cindex(nr);
else
    Ds_11 = 1; Ds_12 = 1;
    Ds_21 = -cindex(nr).*cos(ctheta);
    Ds_22 = cindex(nr).*cos(ctheta);
    Dp_11 = -cos(ctheta); Dp_12 = -cos(ctheta);
    Dp_21 = cindex(nr); Dp_22 = -cindex(nr);
end
```

A.2 HITRAN codes

This section contains some example programs to calculate synthetic spectra using HITRAN

A.2.1 Calculation using line-by-line parameters

```
% Program to calculate absorption coefficient
% of a gas using line by line parameters from HITRAN.
% Assuming high pressures and hence a Lorentzian lineshape.
% All parameters should be extracted from JavaHawks into
% a database
```

```
function abs_coeff = calcAbsCoeff_CO2(lambda,C_co2,T_co2)
nu = 1./(lambda.*100);       % nu in 1/cm if lambda is in 1/m
Tref = 296;             % Temperature of HITRAN data in K
lineshape = zeros(size(nu));
abs_coeff = zeros(size(nu));
p = 1;              % Assume 1 atm pressure
% % % % Load Gas
clear gas_params gamma;
load('CO2.mat') % from javaHawks
ps = C_co2*p;     % Partial pressure of gas in atm
% Frequency shift compensation
gamma = ((Tref/T_co2).^gas_params(:,5))...
.*(gas_params(:,3).*(p-ps) + gas_params(:,4).*ps);
lineshape = zeros(size(nu));
for i = 1:size(gas_params,1)
% Calculate lineshape
    lineshape = gamma(i)./(pi.*(gamma(i).^2...
+(nu-(gas_params(i,2)+gas_params(i,6).*p)).^2));
% Net absorption coefficient - sum of all lines
    abs_coeff = abs_coeff + gas_params(i,1).*lineshape;
end
```

A.2.2 Direct cross section

This example program can be used to directly read absorption cross section from HITRAN.

```
% Script to read IR cross section from HITRAN database
% IR cross section files are 10 character wide fields with 10 fields per
% line.
% There is a header line which tells the conditions under which the cross
% sections are taken.
```

```
% FILENAME is HITRAN cross section with *.xsc extension
function data = readXSection(filename)
fid = fopen(filename,'r');
line = fgetl(fid);
header = textscan(line,'%s');       % Header is now a cell with all the fields
nu_start = str2double(header{1}(2));        % Wave number start
nu_end = str2double(header{1}(3));          % Wave number end
num_points = str2double(header{1}(4));      % Number of points
nu = linspace(nu_start,nu_end,num_points);  % Frequency of xsection data
line_num = 1;
xsectiondata = [];
while(line_num <= ceil(num_points/10));
    line = fgetl(fid);
    xsectiondata = vertcat(xsectiondata,sscanf(line,'%f'));
    line_num = line_num + 1;
end
data = horzcat(nu',xsectiondata);       % Cross section data matrix
fclose(fid);
```